Using UAS optical imagery and SfM photogrammetry to characterize the surface grain size of gravel bars in a braided river (Vénéon River, French Alps)

Daniel Vázquez-Tarrío, Laurent Borgniet, Frédéric Liébault, Alain Recking

Using UAS optical imagery and SfM photogrammetry to characterize the surface grain size of gravel bars in a braided river (Vénéon River, French Alps)

Daniel Vázquez-Tarrío* [1, 2, 3], Laurent Borgniet[1], Frédéric Liébault[1] and Alain Recking[1]

*Corresponding author. Tel.: (+33) 442971500. vazqueztarrio@cerege.fr

[1]Université Grenoble Alpes, Irstea, UR ETNA, 2 rue de la Papeterie-BP 76, F-38402 St-Martin-d'Hères, France

[2]Fundación para el Fomento en Asturias de la Investigación Científica Aplicada y la Tecnología (FICYT), c/ Cabo Noval, nº11, 1º C, 33007 Oviedo, Spain

[3]Centre européen de recherche et d'enseignement de géosciences et de l'environement (CEREGE), CNRS UMR 7330, Europôle de l'Arbois, BP 80, 13545 Aix-en-Provence, France

Abstract

This paper explores the potential of unmanned aerial system (UAS) optical aerial imagery to characterize grain roughness and size distribution in a braided, gravel-bed river (Vénéon River, French Alps). With this aim in view, a Wolman field campaign (19 samples) and five UAS surveys were conducted over the Vénéon braided channel during summer 2015. The UAS consisted of a small quadcopter carrying a GoPro camera. Structure-from-Motion (SfM) photogrammetry was used to extract dense and accurate three-dimensional point clouds. Roughness descriptors (roughness heights, standard deviation of elevation) were computed from the SfM point clouds and were correlated with the median grain size of the Wolman samples. A strong relationship was found between UAS-SfM-derived grain roughness and Wolman grain size. The procedure employed has potential for the rapid and continuous characterization of grain size distribution in exposed bars of gravel-bed rivers. The workflow described in this paper has been successfully used to produce spatially continuous grain size information on exposed gravel bars and to explore textural changes following flow events.

Keywords: SfM, photogrammetry, grain size, roughness, braided rivers, gravel bed rivers

1. Introduction

Grain roughness and grain size distribution (GSD) of riverbed sediment in gravel-bed rivers have been a long-standing focus of interest for fluvial scientists (Rice and Church, 1998, 2010). On the one hand, grain roughness influences flow resistance, the variability and magnitude of shear stress (Naot, 1984; Robert et al., 1992) and the sediment supply of bedload transport (Paola and Seal, 1995; Vericat et al., 2008), and it is an important parameter in hydraulic modelling (Milan and Heritage, 2012). On the other hand, GSD exerts a significant control on the habitat of many benthic organisms.

In gravel-bed streams, grain size and surface roughness shows substantial heterogeneity at different scales (Leopold et al., 1964; Bluck, 1976; Lisle and Madej, 1992; Ashworth, 1996; Rice and Church, 2010; Milan, 2013; Storz-Peretz and Laronne, 2013; Guerit et al., 2014). At the reach scale, it may be represented by patches or facies of similar texture and grain size (Dietrich et al., 2005; Nelson et al., 2009), defining a textural mosaic. This sedimentary mosaic is particularly complex in braided settings, where the spatial distribution of patches reflects the main morphological components of the braided landform (Storz-Peretz and Laronne, 2013; Guerit et al., 2014).

Development of a completely satisfactory method for measuring grain size and surface roughness in gravel-bed rivers (Hodge et al., 2009a) has been made difficult by the multiscale heterogeneity of riverbed sediment. The most widely followed procedure by fluvial scientists has been the grid-by-number Wolman count (Wolman, 1954; Rice and Church, 1996; Bunte and Abt, 2001). Surface grain size has also been measured using the photosieving approach, which uses high-resolution close-range imagery (taken 1–2 m above ground level) and image processing techniques (Ibekken and Schleyer, 1986; Butler et al., 2001; Rubin, 2004; Graham et al., 2005; Buscombe, 2008; Detert and Weibrecht, 2013). However, while these methods provide rapid and objective ways for sampling grain size, they are best suited for patch-scale studies (Heritage and Milan, 2009; Milan and Heritage, 2012; Woodget, 2015). This is because a large number of samples is needed for a complete characterization of the large-scale sedimentary mosaic (Woodget, 2015). Consequently, fluvial scientists and engineers require a more rapid and objective technique that is capable of providing fast, continuous, and accurate grain size measurements at river reach scales (a few hundred meters in length).

Remote sensing approaches have revolutionized the production of fluvial topographic data over the last two decades (Hohenthal et al., 2011; Brasington et al., 2012), and these new technologies could deliver a satisfying alternative to the classical ways of measuring grain size and surface roughness (Heritage and Milan, 2009; Brasington et al., 2012; Woodget, 2015). Carbonneau et al. (2004, 2005), Verdu et al. (2005), Dugdale et al. (2010), and Tamminga et al. (2014) have successfully employed high-resolution aerial imagery and image texture analysis for grain size determination over large areas, the so-called aerial photosieving approach. This method depends on high-resolution images and light conditions as well as sediment color and texture, and they are limited by pixel size and the need for field calibration (Carbonneau et al., 2005; Verdú et al., 2005). Dugdale et al. (2010) used manual calibration performed directly on the aerial images to replace field data. However, a systematic bias was identified in their results, leading to a consistent overestimation of median grain size. Aerial-image calibration is restricted by the user's ability to discriminate smaller size classes and by pixel bleeding effects (lighter colored stones falsely illuminate adjacent pixels, resulting in clasts appearing to be larger than they actually are). Another alternative approach is based on the use of terrestrial laser scanning (TLS). Several recent studies demonstrate that TLS-derived three-dimensional point clouds provide grain-scale altimetric fields that can be used to infer grain size (Smart et al., 2004; Entwistle and Fuller, 2009; Hodge et al., 2009a, b; Hollenthal et al., 2011; Milan and Heritage, 2012). Based on this, Heritage and Milan (2009) and Brasington et al. (2012) used grain roughness obtained from TLS point clouds to retrieve grain size data in gravel-bed rivers. Also, Milan et al. (2009) and Milan and Heritage (2012) showed grain roughness change maps derived from TLS data. However, TLS surveys are expensive and time-consuming for large-scale applications.

The recent growth and spread of unmanned aerial systems (UASs), coupled with the development and improvement of SfM (Structure from Motion) algorithms (Westoby et al., 2012; Fonstad et al., 2013; Dietrich, 2016; Smith et al., 2016), has enabled the production of highly useful topographic models of fluvial surfaces (Brasington et al., 2012; Micheletti et al., 2014, 2015; Tamminga et al., 2014). The UAS-based SfM photogrammetry provides reconstructions of unvegetated and exposed fluvial topography comparable to those derived by airborne and terrestrial LiDAR (Westoby et al., 2012; Smith and Vericat, 2015), with the main advantage of less expensive equipment. Therefore UAS-based SfM

photogrammetry could seemingly provide high quality, spatially distributed roughness and morphology data that are needed by hydraulic and morphodynamics models (Tamminga et al., 2014). For example, some recent morphodynamic models (i.e., Lauer et al., 2016) considered lateral variations in grain size, and UAS-derived SfM terrain models may have the potential to feed them with the required data in this regard.

This paper reports the testing of optical imagery acquired from UAS in connection with SfM and multiview stereo (MVS) photogrammetry to retrieve the GSD of surface bed sediment in a braided gravel-bed river (Vénéon River, French Alps). As it was already mentioned above, previous TLS experiments (Aberle and Smart, 2003; Heritage and Milan, 2009; Brasington et al., 2012) showed that surface roughness computed from 3D point clouds can be used as a proxy of grain size in gravel beds. Here we followed the same approach, using instead SfM-derived point clouds. Three main objectives guided this research: (i) determine the best roughness metric for a percentile estimate from 3D point clouds; (ii) explore whether capturing the spatial variability of surface grain size is possible from distributed roughness information; and (iii) investigate whether detecting changes in surface grain size from roughness information is feasible.

2. Study site

The Vénéon River is a tributary to the Romanche River in the Southern French Alps, draining a 316-km^2 catchment in the Ecrins Massif (Figs. 1A, B). The physical landscape of the basin is dominated by steep rocky slopes, colluvium deposits, and modern and relict periglacial and glacial landforms. Current climate conditions are those typical of a continental, relatively dry and cold climate. The main water source of the Vénéon is La Pilatte glacier, determining a glacial-nival hydrological regime, with the highest discharges between May and August related to snow and glacier melting. High-magnitude flood discharges are related to high temperatures combined with the occurrence of storm-induced heavy rainfalls. The lowest discharges occur between January and March when snowfall dominates. An EDF (Electricité de France) gauging station that has gathered data from 1989 to the present is located upstream of the study site. The mean hourly discharge of this gauging record is 12 $m^3 s^{-1}$, while the maximum and minimum hourly discharges are 206 and 0.1 $m^3 s^{-1}$, respectively. The estimated biannual and decadal peak discharges are 110 and 168 $m^3 s^{-1}$, respectively.

The study reach comprises a 2.5-km-long and 100- to 200-m-wide river reach where the Vénéon develops a braided planform (Fig. 1C). This braided channel is located upstream of a major obstruction related to a large left-bank rock avalanche deposit. The mean channel slope is 0.013. The catchment area at the study reach is 235 km^2. Two single dominant channels can generally be distinguished within the overall braided plain. Several seasonal bar-top channels that cut bar surfaces are present. Water flows permanently in the two main anabranches, while bar-top channels are only active during summer high flow events. A 20-m-high hydropower dam (the *Plan du Lac* dam) was built between 1941 and 1943 immediately downstream of the study reach (Fig. 1). This hydropower dam is managed by EDF.

Bed sediment of the study site is mainly composed of well-rounded and subspherical granitic and metamorphic gravels and cobbles. On exposed gravel bars, the bed sediment is randomly packed, exhibiting a 'normally loose' state (*sensu* Church, 1978) without strong imbrication or well-developed grain arrangements (e.g., clusters, stone lines). Discrete small patches (decametric to metric scales) of sand and fine gravel are spread throughout the coarse framework of gravel bars. Conversely, the underwater channel is depleted in sand sediment; and the bed state is 'underloose', composed mainly of closely packed and imbricated coarse particles and grain structures.

3. Material and methods

3.1. Field data acquisition

3.1.1. UAS surveys

Five UAS flights were carried out over the study reach between April and July 2015 using the same unmanned vehicle, a rotatory-wing quadcopter equipped with a GPS for automate flights (Fig. 1C). The capabilities of the vehicle were limited to favorable weather conditions (no rain, wind velocity up to 11 m s^{-1}). Flight height was ~30 m, and the average flight velocity was ~5 m s^{-1}. Images were taken at 1-s intervals using a GoPro HERO 3+ Silver camera (2.77 mm focal length) that was mounted on a platform in the base of the quadcopter. Images were recorded with a resolution of 5 Mpx (2624 × 1968 pixels), using a narrow field of view (28 mm equivalent focal length).

The SfM-derived point clouds were georeferenced using a set of 92 ground control points (GCPs; Fig. 1C) marked along the study reach using a target design automatically detected by the photogrammetric software (AgiSoft PhotoScan). The targets were deployed in the field and this operation took between 1

and 2 hours before every flight. To save time during the successive drone surveys, target positions were marked with paint in those areas overlapping over consecutive flights. The GCP coordinates were measured in the RGF Lambert 93 coordinate system (EPSG 2154) using a dGPS in RTK (Real Time Kinematic) mode (10 s). A unique position of the dGPS receiver was chosen on an elevated point covering the whole study reach, where good satellite constellation coverage was achieved. Furthermore, to increase the accuracy of dGPS data, the coordinates of the receiver position were referred to those of a permanent geodetic point from the IGN (National Geographic Institute) network during post-processing.

3.1.2. Pebble counts on exposed gravel bars

A data set of 19 Wolman pebble counts was collected in the study reach. These samples were taken between March and May 2015 on exposed gravel bars (Fig. 1C). Sample locations were chosen to be representative of the dominant sediment facies. Each pebble count consisted of 100 grains collected along two ~50 m sampling lines spaced ~5 m apart. Sampling of grains was done systematically, extracting them at every 1 m intersection along a tape (around twice the largest grain size visually estimated in the field). To minimize the operator's bias, all the grains were selected and measured by the same person. Metallic templates were used to measure the *b*-axis of grains > 8 mm and to classify them into half-Ψsize classes. Smaller grains were classified into two groups: grains between 4 and 8 mm and grains <4 mm. In addition, the coordinates of the central point of each sampling area were measured using a GPS device.

Average D_{50} and D_{84} of exposed gravel bars were 39 and 81 mm, respectively. The average percentage of fine sediment (<8 mm) was 18% (±9%). In addition, GSDs have been truncated at 8 mm, following Rice (1995) who found that particles finer than 8 mm are underrepresented in pebble counts and should consequently not be considered. Average D_{50} and D_{84} of truncated GSDs were 46 and 87 mm, respectively (Fig. 2).

3.2. Point cloud processing

3.2.1. SfM photogrammetry

The UAS images were processed using Agisoft PhotoScan. This software follows the typical steps of SfM-MVS photogrammetry (Remondino et al., 2014). First, it searches for common features across

overlapping images and finds points that are stable under viewpoint. Afterwards it solves the intrinsic and extrinsic orientation parameters of the camera using a bundle-adjustment algorithm (Robertson and Cipolla, 2009; Semyonov, 2011; Verhoeven et al., 2012; Javernick et al., 2014; Woodget, 2015) and uses the Brown model to correct image distortions related to the camera lens (Brown, 1966; Agisoft, 2013; Woodget, 2015). In the third stage, PhotoScan makes a densification of the point cloud using a dense multiview stereo reconstruction.

As a result of this workflow, a dense point cloud in an arbitrary coordinate system is produced. PhotoScan can transform the derived model into the absolute coordinate system. To accomplish this, GCPs should be manually identified and coordinates imported into the user interface (Javernick et al., 2014). In theory, this process only requires a minimum of three GCPs (James and Robson, 2012, 2014); in practice, more GCPs will produce a better registration of the model. Here we used a large number of GCPs (~90) to achieve a good alignment quality. In addition, an optimization transformation to reduce nonlinear distortions and increase the quality of model registration (Agisoft, 2013; Javernick et al., 2014; Woodget, 2015) was applied. The optimization procedure minimizes geometric distortions by using the known GCP positions to refine the camera lens model and realign the images. Then the geometry of the model is rebuilt after the optimization process.

Using the Agisoft PhotoScan workflow and its custom algorithms (Fig. 3), we produced five different SfM point clouds, corresponding to each UAS survey (Fig. 1C). Average point densities ranged from 40 to 900 points/m^2 (Table 1). We also derived an orthophoto mosaic with a 2-cm pixel resolution for each UAS survey.

PhotoScan point clouds were finally post-processed using Cloud Compare (Cloud Compare 2.6.2., 2015). In the first step, we filtered and smoothed each UAS-SfM point cloud. Visual assessment revealed some isolated erroneous points. We used the SOR (Statistical Outlier Removal) and noise filters available on Cloud Compare to remove them: the former removes the outliers from the 3D point cloud; the latter works as a low pass filter, locally fitting a plan around each point and removing the points too far away from the fitted plan.

The planimetric accuracy of 3D point clouds, appraised from the GCPs, is 8–12 cm. To evaluate the altimetric precision, 71 points were measured with a dGPS in RTK mode (10 s) on a gravel bar: the

standard deviation of *Z*-differences between the dGPS and the UAS-SfM data (±5.3 cm) was used as a measure of the vertical precision of the point clouds.

The resolution of the SfM models (position uncertainty of each point in the point clouds) was quantified using the flat surface of a road located on the right bank of the river (Fig., 1C), assuming that on a planar-scanned surface the local difference of the point cloud heights should be 0 (Lague et al., 2013; Smith and Vericat, 2015). For each point belonging to the road, we estimated the average difference of elevation to the mean in a 10-cm moving window. This value was then averaged for all the points located on the road and assumed as a descriptor of point position uncertainty. In this way, we estimated a resolution of ±0.7 cm for the point clouds (Table 1).

3.2.2. Roughness metrics

Different metrics have been used to characterize surface roughness of fluvial sediments. These can be grouped in three different types: (i) roughness height *rh* (Gomez, 1993), the difference in height between the top of the bed sediment and the locally averaged topographic surface; (ii) twice the standard deviation ($2\sigma_z$) of elevations in a given area (Heritage and Milan, 2009); and (iii) the root mean square height (*RMSH*), the standard deviation of heights in a given area for which the average slope has been detrended (Aberle and Smart, 2003; Brasington et al., 2012; Storz-Peretz and Laronne, 2013).

The roughness height was obtained by computing the difference in elevation between each point in the point cloud and the least-squares best-fitting plane computed on its nearest neighbors, within a kernel distance of a specified size. This was achieved using the Cloud Compare roughness tool. To compute the standard deviation of elevations, we first built a regular grid of a given size, and we assigned to each node the standard deviation of elevation for all the points falling within the grid cell. Finally, we estimated the *RMSH* following a procedure similar to Brasington et al. (2012) and Rychov et al. (2012). A regular-size grid was built, and the average elevation value for all the points falling in the cell was assigned to each cell node. Then a Delaunay triangulation was used to interpolate a height mesh from this grid. At that point, we subtracted the value of elevation in the mesh from the elevation data of the SfM point cloud. Finally, we took these differences and built a new grid, assigning to each cell node the standard deviation of the residuals falling in the cell.

Cloud Compare was used to calculate these three different roughness metrics from the SfM point clouds. Once computed, roughness metrics were compared with grain size percentiles to find the best grain size proxy. At the same time, we evaluated different sizes for the kernel radius used for the *rh* estimates and the grid size utilized during the σ_z and *RMSH* computations. We found an optimum radius of 50 cm (two to three times the largest clast) for the roughness heights and 1 m (four to six times the largest clast) for the grid size used to compute σ_z and *RMSH*. The workflow followed to derive a proxy correlation between grain size and surface roughness obtained from UAS-SfM point clouds is summarized in Fig. 4.

4. Results

4.1. Roughness as a proxy of GSD percentiles

Roughness estimates from SfM were compared to the field grain size measurements. Taking the GPS coordinates of the central point of each Wolman sample area, a 25-m radius buffer was defined on ArcGis. Then, using the UAS-derived orthophoto mosaic, each buffer was clipped defining an area covering the same sedimentary facies sampled in the field. Surfaces corresponding to woody debris were manually excluded from the buffer. Each defined polygon was used as a mask to extract the data from the roughness clouds. The cumulative distributions of the extracted roughness values were computed and the different percentiles were obtained from these distributions.

The D_{50} correlates with median roughness values (Fig. 5): statistically significant (95% confidence level) linear correlations were found between the different roughness estimates and the median grain size, except for the *RMSH* in the nontruncated case. Roughness heights exhibited the strongest correlation with median grain size, while *RMSH* showed the weakest fit. The strength of correlation was higher when using GSDs truncated at <8 mm. Grain size / roughness ratios were around 1:1 with roughness heights, 1:0.5 with σ_z, and between 1:1 and 1:2 with the *RMSH*.

Significant fit was also found between the 84th percentiles of roughness distribution and the D_{84} (Fig. 6). Significant correlations were found with all the roughness metrics (except for *RMSH* in nontruncated cases), but the best fit was found again with *rh* in the truncated GSD. With the 16th percentiles, significant correlations were only found in the truncated GSD with *rh* and the σ_z (Fig., 7). Correlation is lacking in the nontruncated GSD for the 16th percentile with the three roughness parameters. Yet again,

for the 16th and the 84th percentiles, the grain size / roughness ratios are close to 1:1 with roughness heights, 1:1–2 for *RMSH*, and 1:0.5 for σ_z.

The previous results show that correlation between roughness and grain size is stronger when considering truncated GSD. The random elevation error in our point clouds is 0.7 cm on flat surfaces. As a consequence, the real protrusion and roughness elevation of particles smaller than ~1 cm may be masked by the intrinsic noise of the SfM reconstructions. Then we can be consider that SfM roughness is somehow truncated at the fine terms of the GSD, and this may explain why the correlation is stronger when using the <8-mm truncated GSDs.

4.2. Sensitivity analysis

Several issues should be considered in order to understand how to produce a good proxy correlation between roughness and grain size. These concern the number of samples required to calibrate the regression model, the influence of point cloud density in the strength of the correlation, and whether or not field calibration would be needed after each flight.

Therefore, one important issue concerns how many pebble counts are required to calibrate the regression model. Using the mean and standard deviation of our Vénéon's roughness data, a log-normal probability distribution of 3000 roughness values was built (considering *rh* as roughness parameter). Later, the regression model correlating *rh* to D_{50} (regression equation in Fig. 5D) was applied to each *rh* value of the random roughness distribution, and then a matched distribution of 3000 Wolman D_{50} was derived. To take into account the effect of the uncertainty in our roughness-D_{50} fit, we introduced in these simulated D_{50}-samples a gaussian random error equal to the residual standard error of our regression model. Afterwards an increasing number of paired *rh*-D_{50} data was randomly selected; and then the regression was repeatedly run to see how the slope coefficients of the regression equation change as a function of sample number. This simulation was repeated 1000 times. The results of the analysis are presented in Fig. 8A: this plot shows a change of slope in the plot around 8-10 samples. Above this number, slope coefficient of the regression converges to the experimental one, and further increases in the number of samples only involve small changes in the slope coefficient of the regression equation. So, 8-10 samples may be considered as an optimum number of Wolman counts required to calibrate the roughness-grain size fit.

Later, the influence of point density in the strength of the roughness-grain size fit was also assessed. The point clouds were resampled at different point densities and tested how the R^2 of the regression model varies with point cloud density. Fig. 8B shows how the strength of the regression decreases quickly below average point densities around 10–15 points/m^2.

Finally, we also evaluated whether the calibration between roughness height and grain size is flight dependent or not. Data from the first UAS survey (April) were compared with data obtained during the last survey (July): no differences were observed in the regression lines between April and June; and the data from the five UAS flights plot close to both regression lines, independently of the date of the drone survey (Fig. 9A). This suggests that the calibration is not flight dependent. To check this impression more quantitatively, the regression was run individually for each UAS flight data, and the obtained fit was applied to predict grain size for the other four UAS flight subsamples. Predicted D_{50} were plotted versus the measured D_{50} (Fig. 9B) and the plots project very close to the $x = y$ line. This suggests how well the regression equation obtained for each drone flight predicts the grain size-roughness fit in not overlain areas, at least in those covered by the other four UAS flights. This also involves the shape of the regression, which is not substantially different between the five drone flights.

4.3. Applications of the method: mapping surficial GSD and detecting changes after flow events

4.2.1. GSD mapping of exposed gravel bars

The UAS-SfM point clouds have been used to derive grain size maps based on surface roughness metrics (Fig. 10). Once surface roughness was estimated, we sorted point clouds into regular grids (1×1 m) and assigned to each cell the median roughness value for the points falling into the grid cell. We used *rh* as the roughness metric. Then we applied the calibration law between the median roughness and the median grain size, and as a final step we reclassified the size estimates according to the Wentworth grain size scale (Wentworth, 1922).

In this way, we derived grain size charts for April and June 2015 with 1×1-m grid cells. These maps were not quantitatively validated, but visual assessment revealed that the results were coherent with textures of exposed gravel bars visible on images (Fig. 11). The derived grain size maps are restricted to the exposed gravel bar surfaces, and they exclude the areas of woody debris where surface roughness is not directly related to grain-scale topography. In general, the areal extents of the different grain size

classes were very similar in April and June (Fig. 12). Nevertheless, the percentage of sand-to-fine gravels and boulders were slightly lower in June, while the areal coverage of medium and coarse gravels was slightly larger. Indeed, differences in GSDs inferred from April and June grain size maps are statistically significant ($p < 0.01$, Wilcoxon test).

4.2.2. Detection of surficial GSD changes after a flow event

Sequential UAS data can be also used to link morphological and textural changes following floods. Two UAS surveys (10 April and 11 June 2015) were used to detect changes after a 42-m^3 s^{-1} flow event that occurred between 1 and 7 May 2015 (Fig. 13). During this event, the bar-top channels and some marginal areas of gravel bars were flooded. Various morphological adjustments on the surface of the exposed bars and channel margins were induced by this flow event. These data were used to explore whether the elevation changes were related to roughness adjustments on the surface of gravel bars.

Grain roughness maps were built from April and June UAS-SfM data. Point clouds were sorted into regular grids (1×1 m), and we assigned to each pixel the median roughness value using the *rh* metrics. Then, by subtracting the April and June roughness grids, a map of surficial roughness change was produced. A level of detection was applied to the map using the following equation for error estimation:

$$U = 1.96 \cdot \sqrt{2\sigma^2} \quad (1)$$

where U is the uncertainty in roughness change estimation, and σ is the resolution of the SfM point clouds defined from a flat scanned surface (section 3.2.1). Parameter U was then used as a threshold for roughness change detection. The obtained U was 19 mm, below the median roughness and average D_{50} of Vénéon gravel bars (31 and 39 mm, respectively). This value was subtracted from all the cells in the model of roughness differences to derive a map of significant roughness change (Fig. 14). An average roughness variation of −1.6 mm (standard deviation, 36.0 mm) was obtained.

To better evaluate the detected roughness adjustments, these should be compared with morphological changes (Fig. 14). The use of sequential 3D data sets to evaluate geomorphological changes requires multitemporal point cloud alignment (Lallias-Tacon et al., 2014). An alignment operation was performed between the April and June point clouds with the automatic iterative closest point (ICP) algorithm from Cloud Compare by selecting common stable surfaces. This method is often used for

alignment of adjacent scans of terrestrial and airborne LiDAR (Lallias-Tacon et al., 2014) and sometimes for fusion of airborne and terrestrial LiDAR point clouds (Iavarone and Vagners, 2003; Rabatel et al., 2008; Theule et al., 2012). After the alignment process, the average difference in elevation between common stable areas was 1 mm.

Based on the recorded point clouds, DEMs were constructed with ArcGIS following a simple workflow in which ground points and inverse weighted distances were used to derive a triangular irregular network (TIN), which was then linearly resampled on a 0.25-m grid. A DEM of differences (DoD) was calculated by subtracting the June elevations from April elevations on a cell-by-cell basis. Several studies (Heritage et al., 2009; Wheaton et al., 2010; Milan et al., 2011) have demonstrated the importance of accounting for spatially distributed errors across a DEM surface. Spatially distributed errors were accounted here following the protocol suggested by Lallias-Tacon et al. (2014), based on Milan et al. (2011). This procedure estimates spatially distributed errors in the DoD by separating errors induced by the photogrammetric survey and errors induced by interpolation method used to produce the DEM. The level of detection (LoD) of altimetric change can then be propagated into the DoD from:

$$LoD = 1.96 \cdot \sqrt{\left(\sqrt{\sigma_{sur\,Avril}^{\,2} + \sigma_{\mathrm{int}\,Avril}^{\,2}}\right)^2 + \left(\sqrt{\sigma_{sur\,June}^{\,2} + \sigma_{\mathrm{int}\,June}^{\,2}}\right)^2} \qquad (2)$$

where σ_{sur} is the altimetric error and σ_{int} the interpolation error. As already pointed out in section 3.2.1, the altimetric error (5.3 cm) was estimated from the comparison with dGPS data. Interpolation errors were estimated from a regression equation established between the standard deviation of elevation error (difference between SfM points and DEM pixel elevations) and topographic roughness. Equation (2) defines the minimum LoD for a significant elevation change between April and October.

The thresholded DoD shows an average elevation change of 5 cm (standard deviation, ±25 cm). Patches of scour and fill are spread throughout the surface of compound bars, covering roughly 30% of the exposed surface (9% scour, 21% fill). The thresholded DoD was compared to the model of roughness variations (Fig. 14). While different directions of change in grain roughness were found for the scoured and filled surfaces, scoured areas show some tendency toward roughness decrease (average change, −19.4 mm, ±49.5 mm). Eroded surfaces were often located on bar platforms, where scouring involved the removal of protruding stones as well as smoothing of sand patches through removal of bedforms (current ripples, megaripples). This should involve a decrease in surface roughness.

5. Discussion

5.1. Roughness as a proxy of GSD

These results show that the *rh* roughness metric provided the best proxy of grain size percentiles. Compared to the σ_z and the *RMSH*, roughness heights are more closely related to the actual protrusion of grains on the bed surface: it quantifies the exact difference in height between the top of stones and the average bed surface, while σ_z and the *RMSH* only deliver an averaged measure of grain scale relief in the surrounding area of each stone.

In some of the sample locations, sand and fine sediment occupies pockets between coarse stones. This strong variation in local relief in these interstitial spaces involves high roughness values for the smaller clasts. Also, sand bodies in the Vénéon are often featured by bedforms (current ripples, megaripples), so roughness is more closely related to microforms than to grains in some of these sand patches. Both effects may help to explain why correlation strength decreases for the finer percentiles of the GSDs.

The comparison with previously published TLS-based experiments (Fig. 15) reveals that no universal relation exists between surface roughness and grain size. Our results fall very close to a 1:1 ratio and very close to the *c*-axis plot reported by Heritage and Milan (2009). However, with the Wolman sampling, the *b*-axis was measured. It is often said (Johansson, 1963; Limerinos, 1970; Bathurst, 1982; Gomez, 1993) that the *c*-axis is usually aligned to the vertical, while the *a*- and *b*-axes are preferentially aligned orthogonal and parallel to the main flow direction, respectively (Gomez, 1993; Baewert et al., 2014). Visual assessment in the field of particle shape revealed that clasts are mostly rounded to sub-rounded in the Vénéon. Rounded particles are featured by very similar *c*- and *b*-axis dimensions, and this could explain why the data plot very close to a 1:1 ratio and also to the *c*-axis roughness relations found by Heritage and Milan (2009). Brasington et al. (2012) plotted data between the *c*- and *b*-axis relation given by Heritage and Milan (2009), which could be partially explained by the fact that their data set includes a mixture of rounded and platy particles. In the same vein, Heritage and Milan (2009) found that two patches of similar size and particle shape may have different roughness heights resulting from textural differences. Apart from clast shape, other textural constraints on surface roughness may be packing, variable burial depth of clasts by fines or imbrication angle (Robert, 1990; Heritage and Milan, 2009; Hodge et al., 2009b), as well as bedforms and particle clusters (Brasington et al., 2012).

In summary, while grain size should be one of the major controls on surface roughness in gravel-bed rivers (Hodge et al., 2009b), other factors such as particle shape, grain packing, imbrication, and clustering are also important controls on surface roughness. As a consequence, the grain size–roughness relationship is far from being universal. In each study case, it should be affected in a unique manner by all the textural constraints.

5.2. GSD mapping of exposed gravel bars

Based on UAS-SfM point clouds and using surface roughness metrics, we succeeded in deriving grain size charts of the study site. While these maps were not validated with an independent data set, the visual comparison with high-resolution images (2-cm pixel size) suggests that these GSD charts are quite realistic when compared with the actual surface GSD of gravel bars.

Comparable spatially continuous grain size maps were previously produced based on high-resolution aerial images and image texture analysis (Carbonneau et al., 2005; Verdu et al., 2005; Dugdale et al., 2010; de Haas et al., 2014; Tamminga et al., 2014). This method can potentially deliver continuous grain size maps over large areas (1–80 km) with centimetric precision at spatial resolutions of 1 m^2. However, it is strongly dependent on particle sorting, substrate homogeneity, and scene illumination and requires very high resolution imagery (Brasington et al., 2012). Indeed, the image texture approach is adversely affected by the blurred imagery often acquired from relatively unstable UAS platforms (de Haas et al., 2014; Woodget, 2015). On the contrary, the SfM-roughness approach allows more flexibility on data acquisition, and it also has the potential to provide grain size measurements at finer scales than the image texture analysis, which is restricted by the pixel size of available aerial imagery and pixel bleeding effects when the operator calibrates directly on the aerial images (Dugdale et al., 2010). Additionally, UAS-SfM simultaneously provides highly accurate topographic reconstructions and GSD information of gravel beds, while the image texture approach only delivers grain size information.

However, GSD mapping based on UAS-SfM data sets has two main limitations. One is because of woody debris on gravel bars. On these surfaces, roughness is not related to grain size, but rather to the shape of the log and woody bodies. No grain size information can be retrieved from roughness near these areas. Another disadvantage is the limitation of our GSD charts to exposed gravel bar surfaces. This could be enough for many applications, but in other cases the grain size of submerged areas is also

important. One possible solution is the combination of the UAS-SfM-based method with the conventional Wolman sampling of submerged areas. Nevertheless, Woodget et al. (2015) showed that a refraction correction could be applied on submerged areas on SfM point clouds, and in this way, they obtained information on channel bathymetry in shallow and clear water areas (<0.5 m) with centimetric vertical accuracy comparable to dry bar areas.

While we flew over the Vénéon during overall low-flow conditions, the waters of this river were featured by a characteristic opaque, turquoise color typical of glacier melting flows. Consequently, the information about the submerged areas was lost here. However, results from Woodget et al. (2015) are very promising and suggest that the roughness estimates based on UAS-SfM point clouds could also be applied to shallow, clear water areas.

5.3. Detection of roughness adjustments

The level of detection of significant surface roughness change was estimated at 19 mm. Taking into account that the median grain roughness for Vénéon gravel bars is 31 mm, changes that are smaller than the median roughness of gravel bars can be detected with confidence.

In addition, grain roughness change detection in the Vénéon is only possible for the areas that remained exposed before and after the flow event. Information on underwater GSD changes are lost. However, as we stated above (section 5.2), the results of the Woodget et al. (2015) study suggested that SfM has the potential to be applied to shallow-water submerged areas.

Milan et al. (2009) and Milan and Heritage (2012) were the first to show grain roughness change maps derived from TLS data. They found coarsening in areas of scour and fining in areas of deposition. Conversely, results of the present study show that morphological and roughness changes are not clearly related. Grain roughness changes occurred in the Vénéon without significant elevation changes and vice-versa. Previously, Rice and Church (2010) also found slight grain size adjustments after floods in the wandering Fraser River, with no clear relation between morphological and grain size changes.

5.4. Summary recommendations

Figure 4 graphically summarizes the workflow followed in this study to approach grain size from surface roughness and UAS-SfM point clouds. The results are very encouraging. Applying SfM-MVS photogrammetry to optical images, taken with a low-cost unmanned aerial platform provided with an

inexpensive camera system and flown at a low altitude, we succeeded in obtaining a good regression model correlating surface roughness and grain size.

Related to flight conditions, previous studies by Micheletti et al. (2014) and Smith and Vericat (2015) showed that a ratio of 1:625 to 639 exists between the RMSE of elevation values and flight range. Consequently, strong decreases could be expected in the quality of the roughness reconstruction with flight range. Taking this into account, UAS flights should probably be done at low altitudes (30–50 m) for surface roughness characterization. The sensor utilized for measurements could also have some influence, but this topic is not addressed herein. Probably, the use of a higher-resolution and better-quality camera system would allow increasing flight height. Nevertheless, according to Micheletti et al. (2015) and Smith et al. (2016), no significant differences in the quality of SfM reconstructions should be expected between different sensors flown at flight ranges <100 m. Regarding data processing, it seems that point densities between 15 and 20 points/m^2 are enough for a good characterization of surface roughness for the purpose of grain size mapping. Once high-density SfM point clouds are derived, they can be thinned and density lowered to 15–20 points/m^2, simply to reduce computing time when estimating roughness statistics. This density threshold may be grain size dependent and probably higher in case of gravel beds much finer than those studied here.

From our data, roughness height was found to be the best proxy for grain size. More data is needed to determine if roughness height performs the best for all sediment textures. Additionally, it seems that a textural signature exists in the slope coefficient of the regression equation linking surface roughness to grain size. Field calibration is necessary if SfM roughness is to be used to predict grain size. An important issue concerns the minimum number of samples needed to reach a satisfactory regression model. Here we used 19 Wolman counts to calibrate the regression models, but according to the sensibility analysis, half this number (9 to 10 samples) would have been enough to achieve a reliable fit. This is an affordable number of samples, which could easily be taken over 1–2 days simultaneously with a UAS survey. However, we can easily imagine that the number of samples needed could be influenced by grain size heterogeneity and patchiness. Study cases with a more patched bed texture or grain size heterogeneity could require a larger number of samples.

6. Conclusions

In this paper, UAS optical imagery and SfM photogrammetry were used to characterize grain roughness and GSD of a braided reach in the Vénéon River, a gravel-bed stream located in the French Alps. We showed the potential of this relatively inexpensive method to provide, together with highly dense and accurate topographical reconstruction of fluvial topography, spatially continuous characterizations of grain size.

The results found here confirms that surface roughness computed from dense and accurate UAS-derived SfM point clouds can be used to provide data on the distribution of grain roughness for exposed bar and river bed surfaces. In summary, the results show moderate to strong correlations (0.45-0.90) between surface roughness and the different percentiles of the truncated GSD and the coarser percentiles of the nontruncated GSD (Table 2). In general, the correlation was stronger when using roughness heights as the roughness metric.

We believe that the procedure followed here has great potential for simplifying grain size measurements in gravel-bed rivers by reducing the number of Wolman counts needed to characterize the reach scale GSD. Field calibration is still necessary, to the extent that surface roughness is not only controlled by grain size but also by other textural constraints. Nevertheless, a low number (8-10) of Wolman samples seems to be required; and once the roughness-GSD model for a given stream has been calibrated, running long-term monitoring of grain size and roughness would be possible without the need for a new field sampling. Consequently, the methodology presented in this paper offers a reliable and low-cost solution for the monitoring of the surface texture of exposed gravel bars over stream reaches of a few kilometers' length.

Acknowledgements

The present work has been possible thanks to the financial support provided by the ACA14-30 grant, cofounded by the post-doctoral 'Clarin' program-FICYT (Government of the Principality of Asturias) and the Marie Curie Cofund. This work also benefited from the financial support from EDF and is part of the ZABR LTER network. We are particularly grateful to Remi Loire and Jean-René Malavoi for supporting this project. Special thanks should also be made to Marie Vivier, Gullaume Piton, Emmanuel Thibert, Fred Ousset, Eric Mermin ,and Pascal Tardif for their comments and strong help in the field.

Finally, we would like to acknowledge editor-in-chief Richard Marston, Basil Gomez, and the three anonymous reviewers for their comments that helped to improve the final version of the paper.

References

Aberle, J. and Smart, G. M. (2003). The influence of roughness structure on flow resistance in mountain streams. Journal of Hydraulic Research, 41 (3), 259-269.

Agisoft (2013). Agisoft PhotoScan User Manual: Professional Edition, Version 1.0.0.

Ashworth, P. J. (1996). Channel bar growth and its relations to local flow strength and direction. Earth Surface processes and Landforms, 21, 103-123.

Baewert, H.; Bimböse, M.; Bryk, A.; Rascher, E.; Schmidt, K.-H. and Morche, D. (2014). Roughness determination of coarse grained alpine river bed surfaces using terrestrial laserscanning data. Zeitschrift für Geomorpholgie, 58, Supplementary Issue 1, 81-95.

Bathurst, J.C. (1982). Theoretical aspects of flow resistance. In: Hey, R.D., Bathurst, J.C., Thorne, C.R. (Eds.), Gravel-bed Rivers. Wiley, Chichester, pp. 83–105.

Bluck, B. J. (1976). Sedimentation in some Scottish rivers of low sinuosity. Transactions of the Royal Society of Edinburgh, 69, 425-456.

Brasington, J.; Vericat, D. and Rychov, I. (2012). Modeling river bed morphology, roughness, and surface sedimentology using high resolution terrestrial laser scanning. Water Resources Research 48 W11519.

Brown, D.C. (1966). Decentering distortion of lenses. Photogrammetric Engineering ,32 (3), 444-462.

Bunte, K. and Abt, S.R., (2001). Sampling surface and subsurface particle-size distributions in wadable gravel- and cobble-bed streams for analyses in sediment transport, hydraulics and streambed monitoring. General Technical Report n° RMRSGTR74, U.S. Departement of Agriculture, Forest service, Rocky Mountain Research Station, Fort Collins, Colorado, 428 p.

Buscombe, D. (2008). Estimation of grain size distributions and associated parameters from digital images of sediment. Sedimentary Geology, 210, 1-10.

Butler, J.B.; Lane, S.N. and Chandler, J.H. (2001). Automated extraction of grain-size data for gravel surfaces using digital image processing. Journal of Hydraulic Research, 39, 519–529.

Carbonneau, P.E.; Lane, S.N. and Bergeron, N. (2004). Catchment-scale mapping of surface grain size in gravel bed rivers using airborne digital imagery. Water Resources Research 40, W07202.

Carbonneau, P.E.; Bergeron, N. and Lane, S.N. (2005). Automated grain size measurements from airborne remote sensing for long profile measurements of fluvial grain sizes. Water Resources Research, 41, W11426.

Church, M. (1978). Palaeohydrological reconstructions from a Holocene valley fill. In: Miall, A. (ed.). Fluvial Sedimentology, Can. Soc. Petrol. Geol. Mem., vol. 5, pp., Alberta (Canada), pp. 743–772.

CloudCompare (version 2.6.2) [GPL software] (2015). Retrieved from http://www.cloudcompare.org/

de Haas, T. ; Ventra, D. ; Carbonneau. P. and Kleinhans, M.G. (2014). Debris flow dominance of alluvial fans masked by runoff reworking and weathering. Geomorphology, 217, 165-181.

Detert, M. and Weitbrecht, V. (2013). User guide to gravelometric image analysis by BASEGRAIN. In: Advances in Science and Research, S. Fukuoka, H. Nakagawa, T. Sumi, H. Zhang (Eds.), Taylor & Francis Group, London, pp. 1789-1795.

Dietrich, J. T. (2016). Riverscape Mapping with Helicopter-Based Structure-From-Motion Photogrammetry. Geomorphology, 252, 144–157.

Dietrich, W. E.;Nelson, P. A.; Yager, E.; Venditti, J. G.; Lamb, M. P. and Collins, L. (2005). Sediment patches, sediment supply, and channel morphology. In: Parker, G. and Garcia, M. H. 4th Conference on River, Coastal, and Estuarine Morphodynamics, RCEM 2005, A. A. Balkema Publishers, Rotterdam, pp. 79–90.

Dugdale, S.; Carbonneau, P. and Campbell, D. (2010). Aerial photosieving of exposed gravel bars for the rapid calibration of airborne grain size maps. Earth Surface Processes and Landforms, 35, 627-639.

Entwistle, N.S. and Fuller, I.C. (2009). Terrestrial laser scanning to derive the surface grain size facies character of gravel bars. In Heritage, G.L. and Large, A.R.G. (Eds). Laser Scanning for the Environmental Sciences, Wiley-Blackwell, London.

Fonstad, M. A. ; Dietrich, J.T. ; Courville, B.C. ; Jensen, J.L. and Carbonneau, P.E. (2013). Topographic structure from motion: a new development in photogrammetric measurement. Earth Surface Processes and Landforms, 38, 421–430.

Gomez, B. (1993). Roughness of stable, armored gravel beds. Water Resources Research, 29 (11), 3631-3642.

Graham, D.J.; Reid, I. and Rice, S.P. (2005). Automated sizing of coarse-grained sediments: image-processing procedures. Mathematical Geology 37, 1–28.

Guerit, L. ; Barrier, L. ; Narteau, C. ; Métivier, F. ; Liu, Y. ; Lajeunesse, E. ; Gayer, E. ; Meunier, P. ; Malverti, L. and Ye, B. (2014). The Grain-size Patchiness of Braided Gravel-Bed Streams – example of the Urumqi River (northeast Tian Shan, China). Advances in Geosciences, 37, 27-39.

Heritage, G. and Milan, D. J. (2009). Terrestrial laser scanning of grain roughness in a gravel bed river. Geomorphology, 113 (1), 4-11.

Heritage, G.L., Milan, D.J., G.L., Large, A.R.G., Fuller, I. and Hetherington, D. (2009). Influence of survey strategy and interpolation model upon DEM quality. Geomorphology, 112, 334-344.

Hodge, R. A.; Brasington, J. and K. S.Richards (2009a). *In situ* characterization of grain-scale fluvial morphology using TLS. Earth Surface Processes and Landforms, 34, 954–968.

Hodge, R. A.; Brasington, J. and K. S.Richards (2009b). Analyzing laser-scanned digital terrain models of gravel bed surfaces: Linking morphology to sediment transport processes and hydraulics. Sedimentology, 56, 2024–2043.

Hohenthal, J.; Alho, P.; Hyyppä, J. and Hyyppä, H. (2011). Laser scanning applications in fluvial studies. Progress in Physical Geography 35 (6), 782-809.

Iavarone, A. and Vagners, D. (2003). Sensor fusion: generating 3D by combining airborne and tripod mounted LIDAR data. Proceeding of ISPRS workshop on "Visualization and Animation of Reality-based 3D Models". Int. Arch. Photogramm. Remote. Sens. Spat. Inf. Sci. XXXIV (5/W10), 7.

Ibbeken, H. and Schleyer, R. (1986). Photo-sieving: a method for grain-size analysis of coarse grained, unconsolidated bedding surfaces. Earth Surface Processes and Landforms 11, 59–77.

James, M.R. and Robson, S. (2012). Straightforward reconstruction of 3D surfaces and topography with a camera: accuracy and geosciences application. Journal of Geophysical Research 117, F03017.

James, M.R. and Robson, S. (2014). Mitigating systematic error in topographic models derived from UAV and ground-based image networks. Earth Surface Processes and Landforms, 39, 1413-1420.

Javernick, L.; Brasington, J. and Caruso, B. (2014). Modelling the topography of shallow braided rivers using Structure-from-Motion photogrammetry. Geomorphology, 213, 166-182.

Johansson, C.E. (1963). Orientation of pebble clusters in running water. A laboratory study. Geografiska Annaler, 45A, 85–112.

Lague, D.; Brodu, N. and Leroux, J. (2013). Accurate 3D comparison of complex topography with terrestrial laser scanner: application to the Rangitikei canyon (N-Z). Journal of Photogrammetry and Remote Sensing, 82, 10-26.

Lallias-Tacon, S.; Liébault, F. and Piégay, H. (2014). Step by step error assessment in braided river sediment budget using airborne LiDAR data. Geomorphology, 214, 307-323.

Lauer, J. W.; Viparelli, E. and Piégay, H. (2016). Morphodynamics and sediment 1D (MAST-1D): 1D sediment transport that includes exchange with an off-channel sediment reservoir. Advances in Water Resources, 93 (A), 135-149.

Leopold, L.B.; Wolman, M.G. and Miller, J.P. (1964). Fluvial Processes in Geomorphology. WH Freeman, San Francisco, 522 pp.

Limerinos, J. T. (1970). Determination of the Manning coefficient from measured bed roughness in natural channels. U.S. Geological Survey Water Supply Paper 1898-B.

Lisle, T.E. and Madej, M.A. (1992). Spatial variation in armouring in a channel with high sediment supply. In: Dynamics of Gravel-bed Rivers (Eds P. Billi, R.D. Hey, C.R. Thorne and P. Tacconi), pp. 277–293. John Wiley and Sons, London.

Micheletti, N.; Chandler, J. H. and Lane, S. N. (2014). Investigating the geomorphological potential of freely available and accessible structure-from-motion photogrammetry using a smartphone. Earth Surface Processes and Landforms, 40 (4), 473-486.

Micheletti, N.; Chandler, J. H. and Lane, S. N. (2015). Structure from Motion (SfM) Photogrammetry Photogrammetric heritage. In: Geomorphological Techniques. British Society of Geomorphology, pp. 1-12.

Milan, D.J. (2013). Sediment routing hypothesis for pool-riffle maintenance. Earth Surface Processes and Landforms, 38, 1623-1641.

Milan, D.J. and Heritage, G.L. (2012). LiDAR and ADCP use in gravel-bed rivers: Advances since GBR6. In Church, M., Biron, P. and Roy, A. (Eds) Gravel-bed Rivers: Processes, Tools, Environments, Wiley Blackwell, Chichester.

Milan, D.J., Heritage, G.L.and Entwistle, N. (2009). Detecting grain roughness change and sorting patterns in a gravel-bed river using terrestrial laser scanning. Proceedings of the 33rd IAHR Congress: Water Engineering for a Sustainable Environment, Vancouver, Canada August 10-14, 2009. CD-ROM, IAHR, pp5004-5011.

Milan, D.J., Heritage, G.L., Large, A.R.G. and Fuller, I. D. (2011). Filtering spatial error from DEMs; implications for morphological change estimation. Geomorphology, 125, 160-171.

Naot, D. (1984). Response of channel flow to roughness heterogeneity. Journal of Hydraulic Engineering, 110, 1568–1587.

Nelson, P. A.; Venditti, J. G.; Dietrich, W. E.; Kirchner, J. W.; Ikeda, H.; Iseya, F. and Sklar, L. S. (2009). Response of bed surface patchiness to reductions in sediment supply. Journal of Geophysical Research, 114, F02005.

Paola, C. and Seal, R. (1995). Grain-size patchiness as a cause of selective deposition and downstream fining, Water Resources Research, 31, 1395– 1407.

Rabatel, A.; Deline, P.; Jaillet, S. and Ravanel, L. (2008). Rock falls in high-alpine rockwalls quantified by terrestrial LiDAR measurements: a case study in the Mont Blanc area. Geophys. Res. Lett. 35 (10), L10502.

Remondino, F; Spera, M. G.; Nocerino, E.; Menna, F. and Nex, F. (2014). State of the art in high density image matching. The Photogrammetric Record, 29, 144–166.

Rice, S. (1995). The spatial variation and routine sampling of spawning gravels in small coastal streams. Research Branch, British Columbia Ministry of Forests, Victoria, B.C., Working Paper 06/1995, 41 pp.

Rice, S.P. and Church, M. (1996). Sampling surficial fluvial gravels: the precision of size distribution percentile estimates. Journal of Sedimentary Research, 66, 654–665.

Rice, S. and Church, M. (1998). Grain size along two gravel-bed rivers: statistical variation, spatial pattern and sedimentary links. Earth Surface Processes and Landforms, 23 (4), 345-363.

Rice, S. and Church, M. (2010). Grain-size sorting within river bars in relation to downstream fining along a wandering channel. Sedimentology, 57 (1), 232-251.

Robert, A. (1990). Boundary roughness in coarse-grained channels. Progress in Physical Geography, 14(1), 42 – 70.

Robert, A.; Roy, A. G. and Deserres, B. (1992). Changes in velocity profiles at roughness transitions in coarse-grained channels. Sedimentology, 39, 725–735.

Robertson, D.P., Cipolla, R. (2009). Structure from Motion. In: Varga, M. (Ed.), Practical Image Processing and Computer Vision. John Wiley, Chichester.

Rubin, D.M. (2004). A simple autocorrelation algorithm for determining grain size from digital images of sediment. Journal of Sedimentary Research, 74 (1), 160-165.

Rychov, I.; Brasington, J. and Vericat, D. (2012). Computational and methodological aspects of terrestrial surface analysis based on point clouds. Computers and Geosciences, 42, 64-70.

Semyonov, D., (2011). Algorithms used in Photoscan [Msg 2]. Retrieved May 3. Message posted to www.agisoft.ru/forum/index.php?topic=89.0.

Smart, G.; Aberle, J.; Duncan, M. and Walsh, J. (2004). Measurement and analysis of alluvial bed roughness. Journal of Hydraulic Research, 42(3), 227-237.

Smith M.W. and Vericat D. (2015). From experimental plots to experimental landscapes: topography, erosion and deposition in sub-humid badlands from Structure-from-Motion photogrammetry. Earth Surface Processes and Landforms, 40 (12), 1656-1671.

Smith, M. W.; Carrivick, J. L. and Quincey, D. J. (2016). Structure from motion photogrammetry in physical geography. Progress in Physical Geography.

Storz-Peretz, Y. and Laronne, J. (2013). Morphotextural characterization of dryland braided channels. Geological Society of America Bulletin, 125 (9-10), 1599-1617.

Tamminga, A.; Hugenholtz, C.; Eaton, B. and LaPointe, M. (2014). Hyperspatial remote sensing of channel reach morphology and hydraulic fish habitat using an unmanned aerial vehicle (UAV): A first assessment in the context of river research and management. River Research and Applications, 31 (3), 379-391.

Theule, J.I.; Liébault, F.; Loye, A.; Laigle, D. and Jaboyedoff, M. (2012). Sediment budget monitoring

of debris-flow and bedload transport in the Manival Torrent, SE France. Nat. Hazards Earth Syst. Sci. 12 (3), 731–749.

Verdú, J.M.; Batalla, R.J. and Martinez-Casasnovas, J.A. (2005). High-resolution grain-size characterisation of gravel bars using imagery analysis and geo-statistics. Geomorphology, 72, 73-93.

Verhoeven, G.; Doneus, M.; Briese, C. and Vermeulen, F. (2012). Mapping by matching: a computer vision-based approach to fast and accurate georeferencing of archaeological aerial photographs. Journal of Archaeological Science 39, 2060–2070.

Vericat, D.; Batalla, R. J. and Gibbins, C. N. (2008). Sediment entrainment and depletion from patches of fine material in a gravel-bed river. Water Resources Research, 44.

Wentworth, C.K. (1922). A scale of grade and class terms for clastic sediments. Journal of Geology 30, 377-392.

Westoby, M. J.; Brasington, J.; Glasser, M. J.; Hambrey, M. J.; Reynolds, J. M. (2012). Structure-from-Motion photogrammetry: a low cost, effective tool for geoscience applications. Geomorphology 179: 300–314.

Wheaton, J.M., Brasington, J., Darby, S.E. and Sear, D.A. (2010). Accounting for uncertainty in DEMs from repeat topographic surveys: improved sediment budgets. Earth Surface Processes and Landforms 35, 136–156.

Wolman, M. G. (1954). A method of sampling coarse river-bed material. Transactions of the American Gepphysical Union, 35 (6), 951-956.

Woodget, A. (2015). Quantifying physical river habitat parameters using high resolution UAS imagery and SfM photogrammetry. PhD dissertation, University of Worcester. 387 pp.

Woodget, A. S. ; Carbonneau, P. E. ; Visser, F. and Maddock, I. P. (2015). Quantifying submerged fluvial topography using hyperspatial resolution UAS imagery and structure from motion photogrammetry. Earth Surface Processes and Landforms, 40 (1), 47-64.

Table 1

Summary of the main characteristics of the UAS-SfM point clouds

Source/ UAS survey	Point density (pts/m^2)	Average point distance (cm)	Roughness resolution (cm)
10/04/2015	1052	0.1	0.3
16/04/2015	291	0.8	0.9
11/06/2015	52	3.4	1.3
24/06/2015	45	4.5	-
02/072015	36	6.0	0.3
Mean	**295**	**3.0**	**0.7**

Table 2. R^2 for the regression equation fitting roughness and grain size, for several percentiles of the cumulative distributions.

	Nontruncated GSD			Truncated GSD		
	R. heights	σ_z	RMSH	R. heights	σ_z	RMSH
D_5	0.08	0.02	0.09	0.59	0.36	0.15
D_{16}	0.00	0.04	0.00	0.64	0.45	0.19
D_{25}	0.01	0.04	0.01	0.68	0.58	0.28
D_{50}	0.26	0.35	0.12	0.89	0.66	0.45
D_{75}	0.57	0.43	0.22	0.86	0.58	0.32
D_{84}	0.54	0.35	0.19	0.83	0.51	0.28
D_{95}	0.35	0.10	0.09	0.73	0.28	0.27

CAPTIONS

Fig. 1. (A) Location of the study site in France. B) Location of the Vénéon River in the Ecrins Massif (French Alps). (C) Detailed view of the study site, with positions of Wolman samples and GCPs.

Fig. 2. Data set of GSD measured in the field during this study. (A) All GSD data. (B) Truncated (<8 mm) GSD data.

Fig. 3. Steps followed in Agisoft PhotoScan to derive SfM point clouds from UAS imagery.

Fig. 4. Workflow for estimating grain size from UAS-SfM point clouds, using a regression model calibrated with a few conventional Wolman pebble counts.

Fig. 5. Median GSD value versus the median roughness value. In the upper row, median GSD values are plotted for the nontruncated GSDs; in the lower row, they are plotted for the truncated (<8 mm) GSDs.

Fig. 6. GSD 84^{th} percentile versus roughness 84^{th} percentile. In the upper row, GSD 84^{th} percentiles are plotted for the nontruncated GSDs; in the lower row, they are plotted for the truncated (<8 mm) GSDs.

Fig. 7. GSD 16th percentile versus the roughness 16th percentile. In the upper row, GSD 16th percentiles are plotted for the nontruncated GSDs; in the lower row, they are plotted for the truncated (<8 mm) GSDs.

Fig. 8. (A) Results of the analysis concerning how many pebble counts are required to calibrate the regression model. An increasing number of roughness-D_{50} data were randomly selected, and then we repeatedly ran the regression to analyze how may pebble counts would be required for calibration. In the figure, the maximum and minimum values obtained for the slope coefficient of the regression equation are plotted (after resampling 1000 times for each sample size). (B) Effect of UAS-SfM point cloud density on the correlation coefficient (r^2) between grain size and roughness median percentiles.

Fig. 9. (A) Regression fit between the 8-mm lower truncated D_{50} and the roughness height (rh) obtained for April (solid line) and July (dashed line) data subsamples. (B) Predicted vs. observed D_{50} values.

Fig. 10. Workflow for extracting the grain size maps from the UAS-SfM point clouds.

Fig. 11. Surface GSD chart derived from UAS-SfM point clouds (right). Left, the ortophotograph (2-cm pixel size). Visual inspection shows correspondence between GSD chart and ortophotograph.

Fig. 12. Areal extent of the different grain size classes determined from surface GSD charts.

Fig. 13. Discharge record of the Vénéon River during the period including UAS flights and grain size field sampling. The arrows represent the dates of UAS surveys, and the grey dashed lines represent the period during which Wolman pebble counts were done.

Fig. 14. DoD model (right) and model of roughness changes (left) built for the study site.

Fig. 15. Roughness and grain size data obtained in the current study are compared to TLS data compiled from the scientific literature. (A) Comparison with studies that used the standard deviation of elevation as the roughness descriptor; (B) comparison with data sets that used the detrended standard deviation.

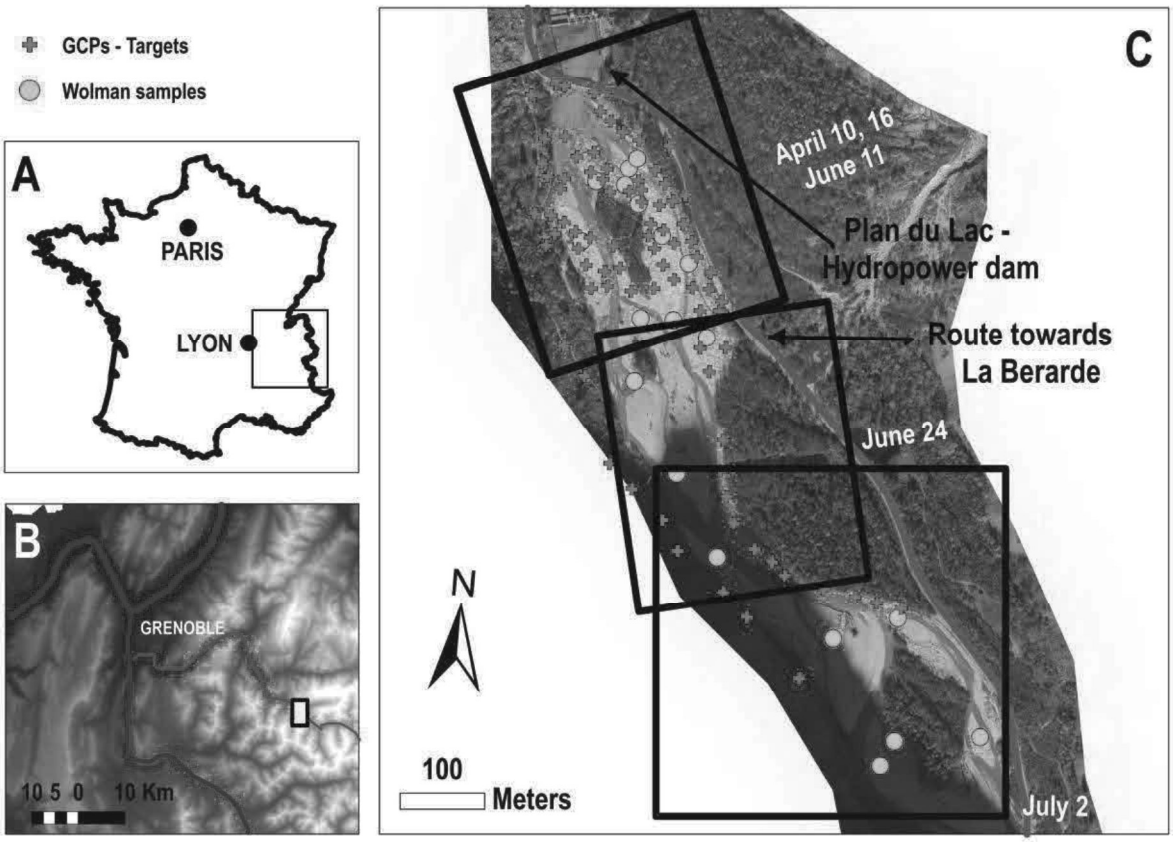
GCPs - Targets
Wolman samples
A
PARIS
LYON
B
GRENOBLE
10 5 0 10 Km
C
April 10, 16
June 11
Plan du Lac -
Hydropower dam
Route towards
La Berarde
June 24
July 2
N
100
Meters

Figure 1.

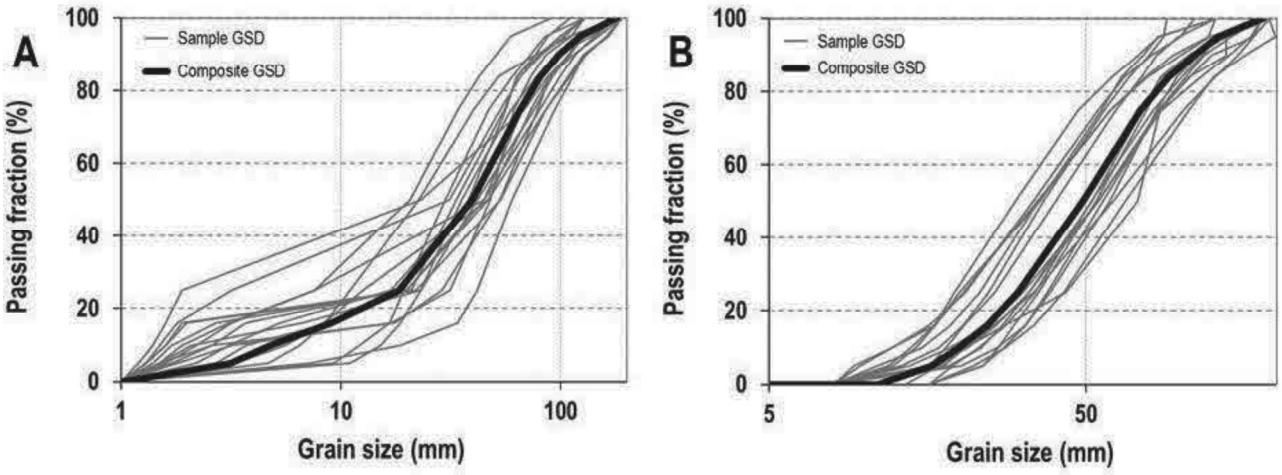
A
Sample GSD
Composite GSD
Passing fraction (%)
100
80
60
40
20
0
1
10
100
Grain size (mm)
B
Sample GSD
Composite GSD
Passing fraction (%)
100
80
60
40
20
0
5
50
Grain size (mm)

Figure 2.

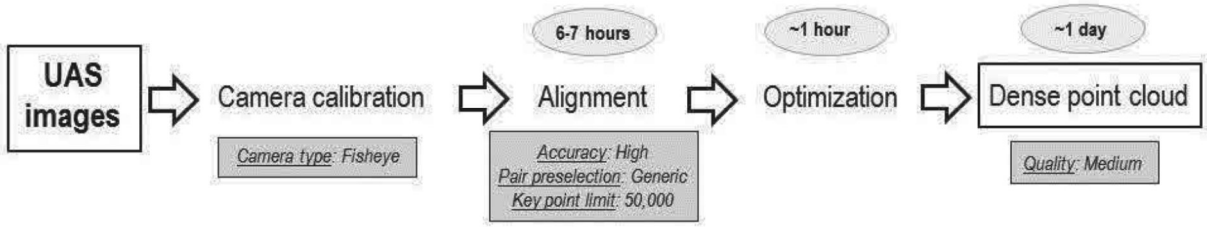
UAS images
Camera calibration
Camera type: Fisheye
6-7 hours
Alignment
Accuracy: High
Pair preselection: Generic
Key point limit: 50,000
~1 hour
Optimization
~1 day
Dense point cloud
Quality: Medium

Figure 3

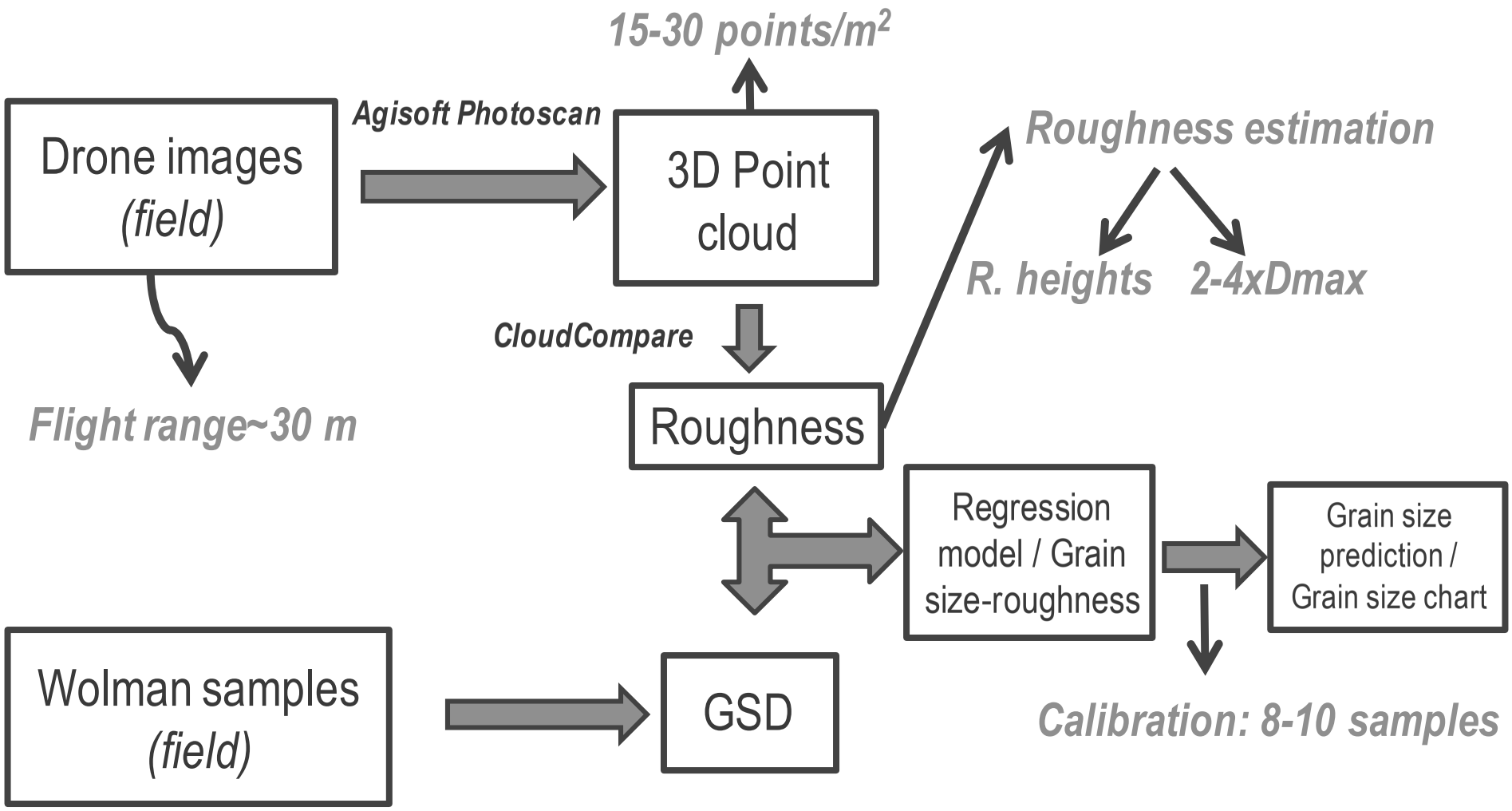
15-30 points/m2
Drone images (field)
Agisoft Photoscan
3D Point cloud
Roughness estimation
R. heights
2-4xDmax
Flight range~30 m
CloudCompare
Roughness
Regression model / Grain size-roughness
Grain size prediction / Grain size chart
Wolman samples (field)
GSD
Calibration: 8-10 samples

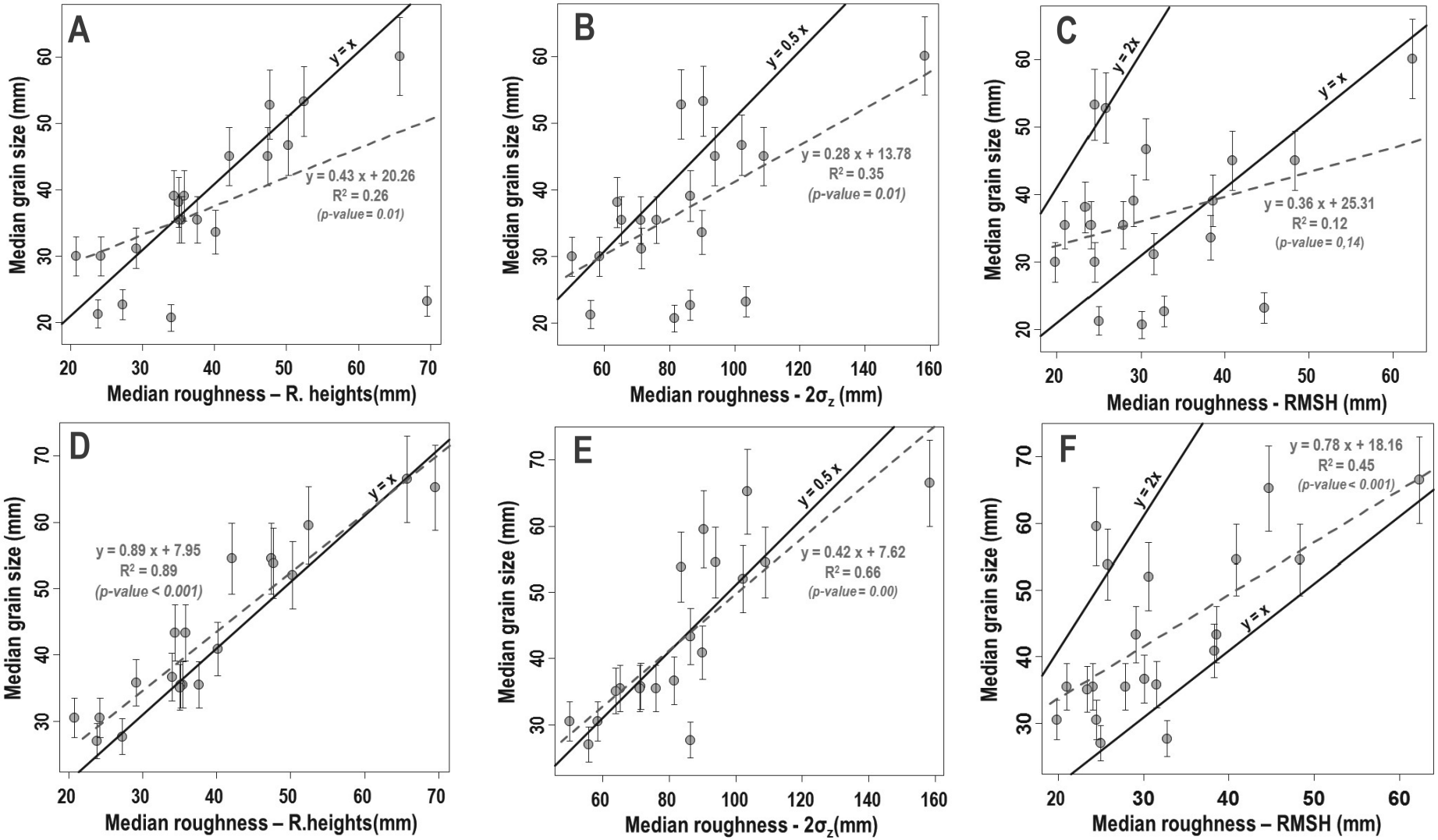
A
y = x
y = 0.43 x + 20.26
R² = 0.26
(p-value = 0.01)
Median grain size (mm)
Median roughness – R. heights(mm)
B
y = 0.5 x
y = 0.28 x + 13.78
R² = 0.35
(p-value = 0.01)
Median grain size (mm)
Median roughness - 2σz (mm)
C
y = 2x
y = x
y = 0.36 x + 25.31
R² = 0.12
(p-value = 0,14)
Median grain size (mm)
Median roughness - RMSH (mm)
D
y = x
y = 0.89 x + 7.95
R² = 0.89
(p-value < 0.001)
Median grain size (mm)
Median roughness – R.heights(mm)
E
y = 0.5 x
y = 0.42 x + 7.62
R² = 0.66
(p-value = 0.00)
Median grain size (mm)
Median roughness - 2σz(mm)
F
y = 2x
y = x
y = 0.78 x + 18.16
R² = 0.45
(p-value < 0.001)
Median grain size (mm)
Median roughness – RMSH (mm)

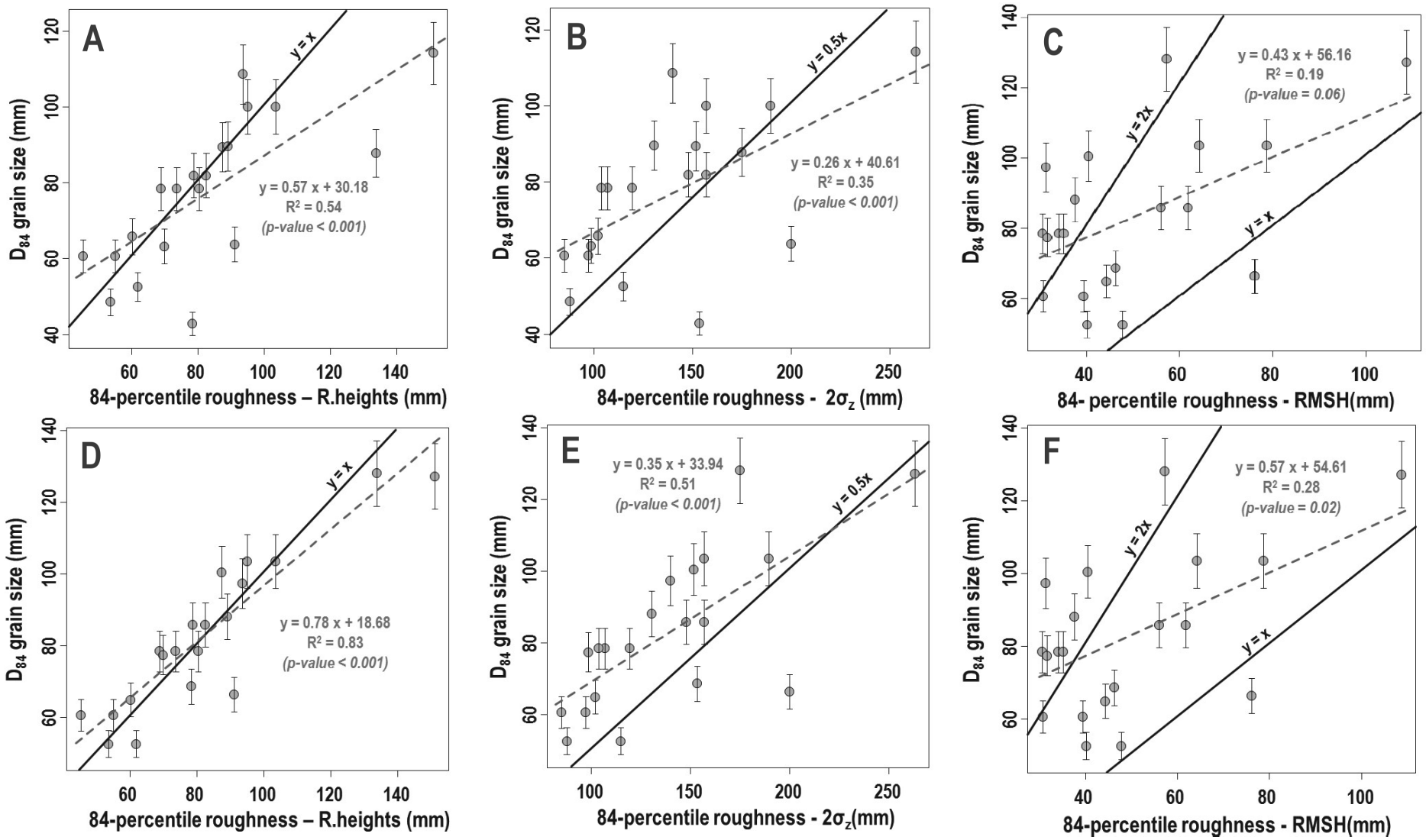
A
y = x
y = 0.57 x + 30.18
R² = 0.54
(p-value < 0.001)
D84 grain size (mm)
84-percentile roughness – R.heights (mm)
B
y = 0.5x
y = 0.26 x + 40.61
R² = 0.35
(p-value < 0.001)
D84 grain size (mm)
84-percentile roughness - 2σz (mm)
C
y = 0.43 x + 56.16
R² = 0.19
(p-value = 0.06)
y = 2x
y = x
D84 grain size (mm)
84- percentile roughness - RMSH(mm)
D
y = x
y = 0.78 x + 18.68
R² = 0.83
(p-value < 0.001)
D84 grain size (mm)
84-percentile roughness – R.heights (mm)
E
y = 0.35 x + 33.94
R² = 0.51
(p-value < 0.001)
y = 0.5x
D84 grain size (mm)
84-percentile roughness - 2σz(mm)
F
y = 0.57 x + 54.61
R² = 0.28
(p-value = 0.02)
y = 2x
y = x
D84 grain size (mm)
84-percentile roughness - RMSH(mm)

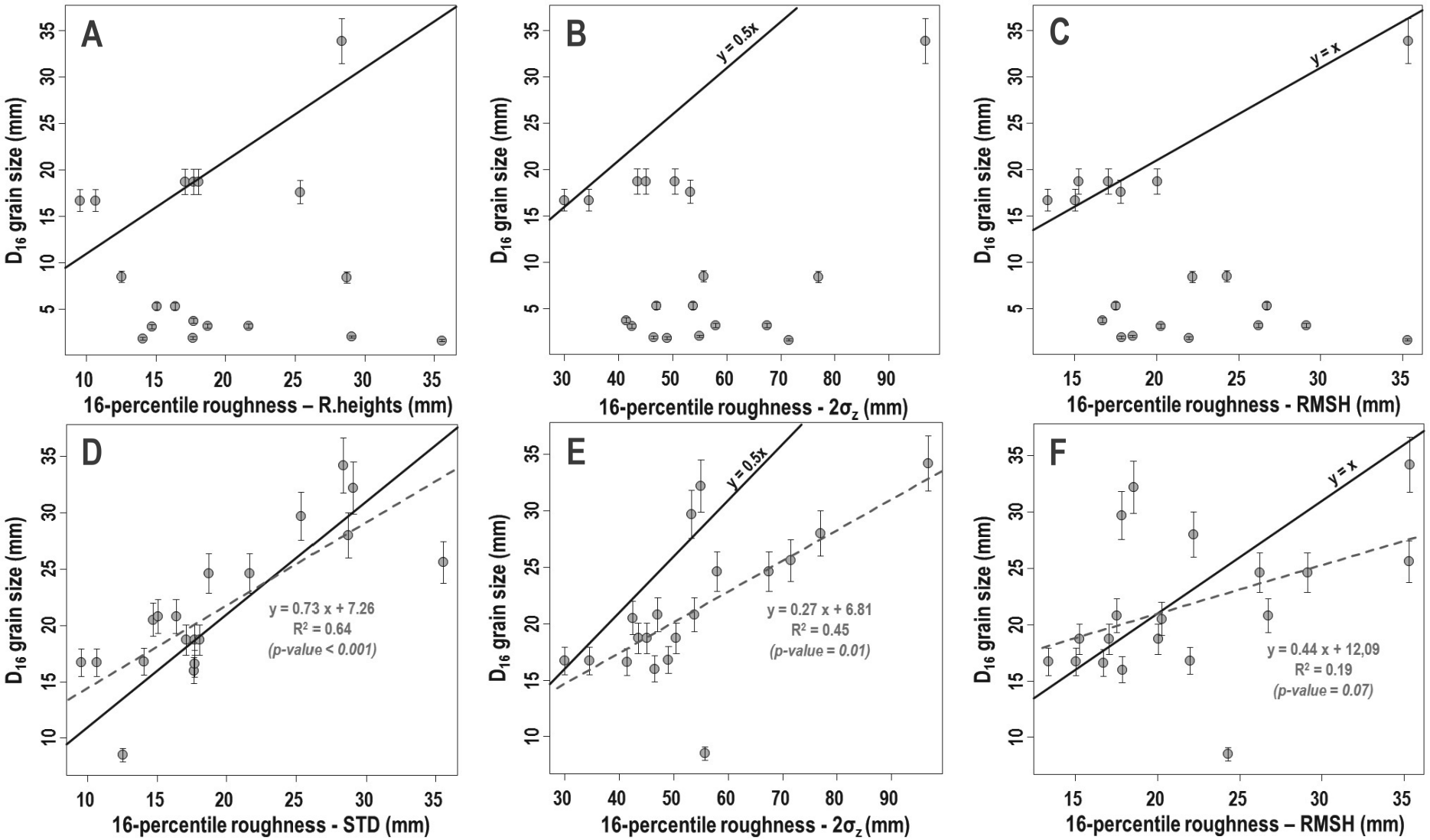
A
B
C
D
E
F
D_{16} grain size (mm)
16-percentile roughness – R.heights (mm)
16-percentile roughness - $2\sigma_z$ (mm)
16-percentile roughness - RMSH (mm)
16-percentile roughness - STD (mm)
16-percentile roughness – RMSH (mm)
y = 0.5x
y = x
y = 0.73 x + 7.26
R^2 = 0.64
(p-value < 0.001)
y = 0.27 x + 6.81
R^2 = 0.45
(p-value = 0.01)
y = 0.44 x + 12,09
R^2 = 0.19
(p-value = 0.07)

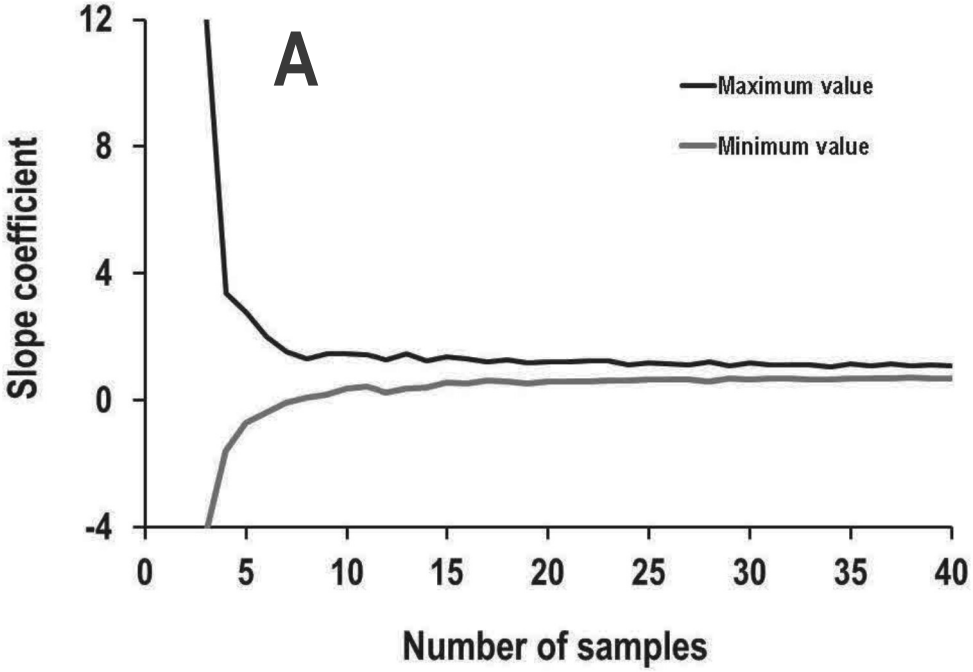
A
Maximum value
Minimum value
Slope coefficient
12
8
4
0
-4
0
5
10
15
20
25
30
35
40
Number of samples

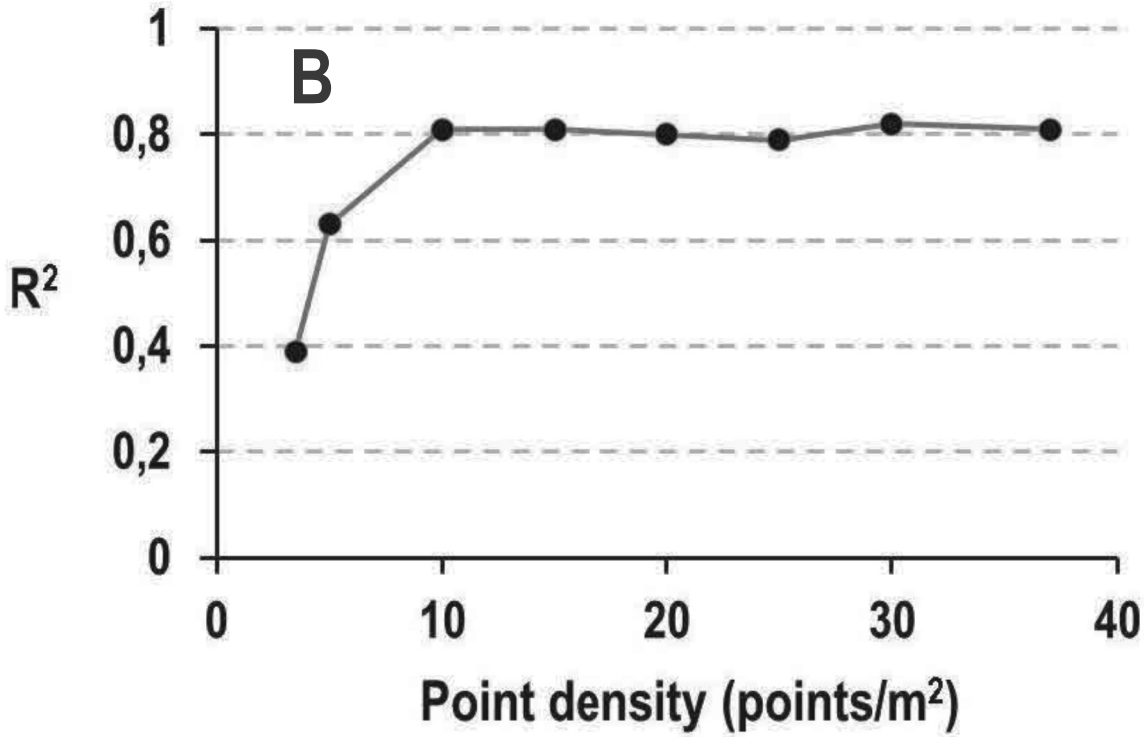
B
R²
1
0,8
0,6
0,4
0,2
0
0
10
20
30
40
Point density (points/m²)

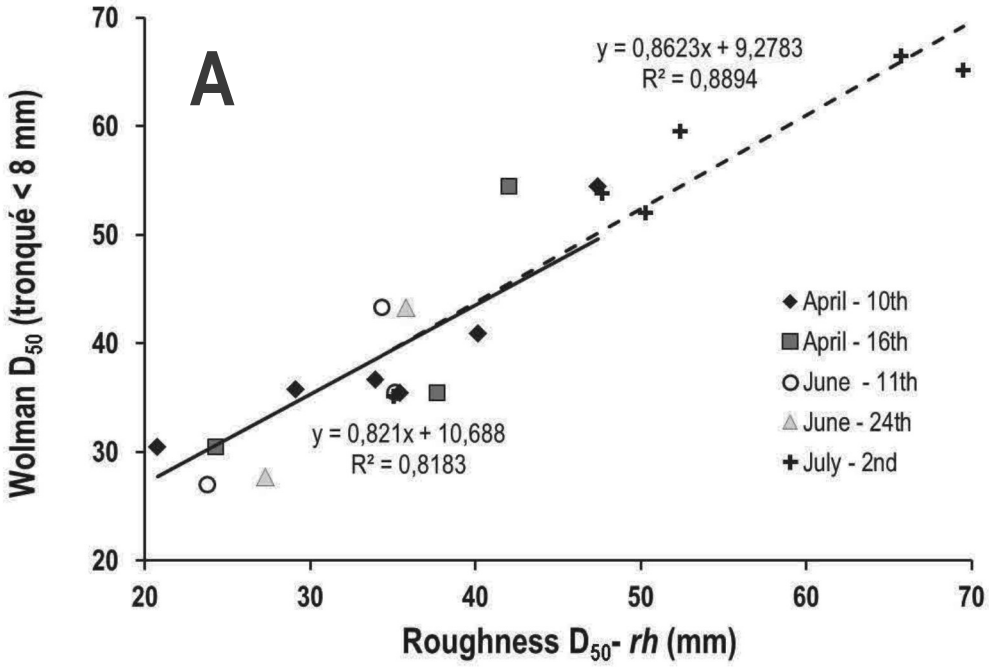
A
y = 0,8623x + 9,2783
R² = 0,8894
y = 0,821x + 10,688
R² = 0,8183
April - 10th
April - 16th
June - 11th
June - 24th
July - 2nd
Wolman D50 (tronqué < 8 mm)
Roughness D50- rh (mm)
20
30
40
50
60
70

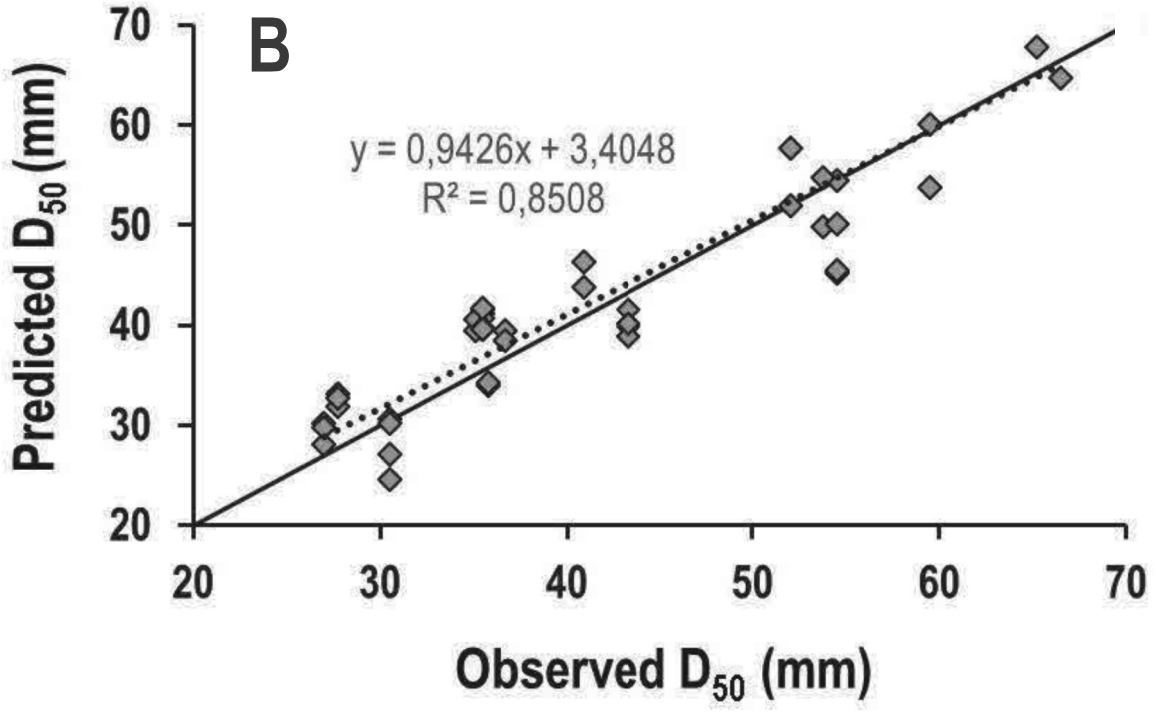
B
y = 0,9426x + 3,4048
R² = 0,8508
Predicted D50 (mm)
Observed D50 (mm)
20
30
40
50
60
70

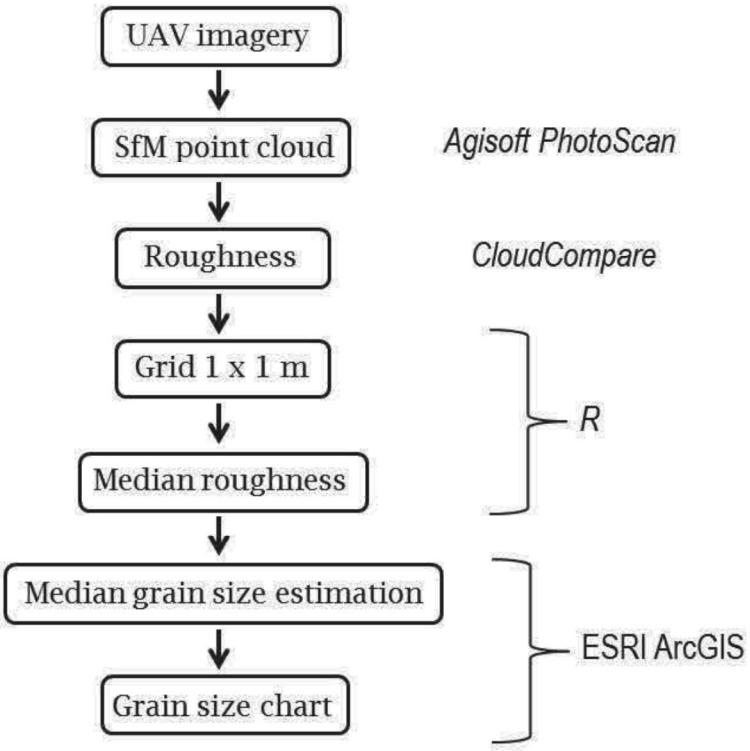
UAV imagery
SfM point cloud
Agisoft PhotoScan
Roughness
CloudCompare
Grid 1 x 1 m
R
Median roughness
Median grain size estimation
ESRI ArcGIS
Grain size chart

Figure 10

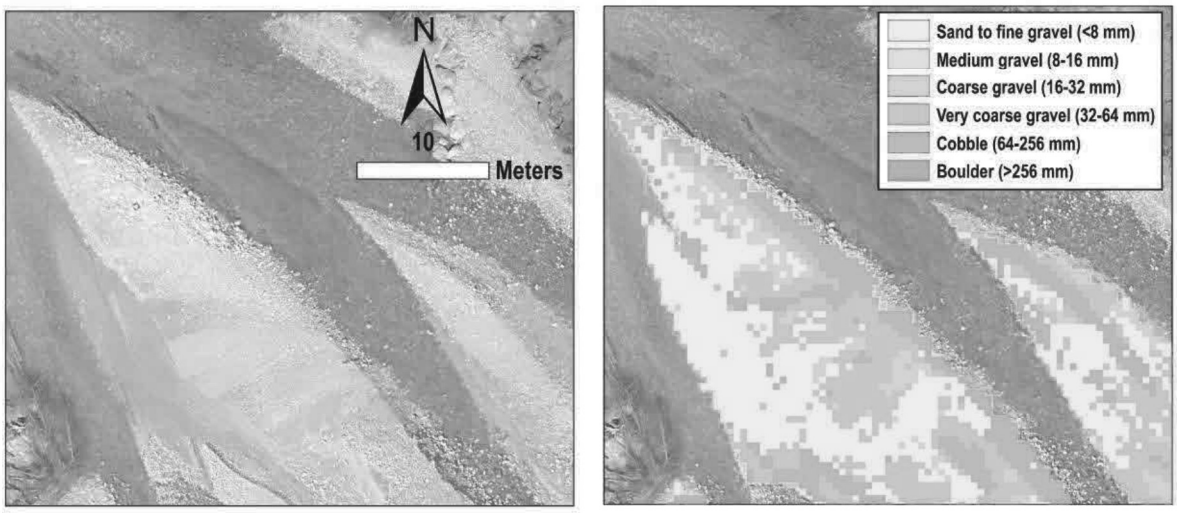
N
10
Meters
Sand to fine gravel (<8 mm)
Medium gravel (8-16 mm)
Coarse gravel (16-32 mm)
Very coarse gravel (32-64 mm)
Cobble (64-256 mm)
Boulder (>256 mm)

Figure 11

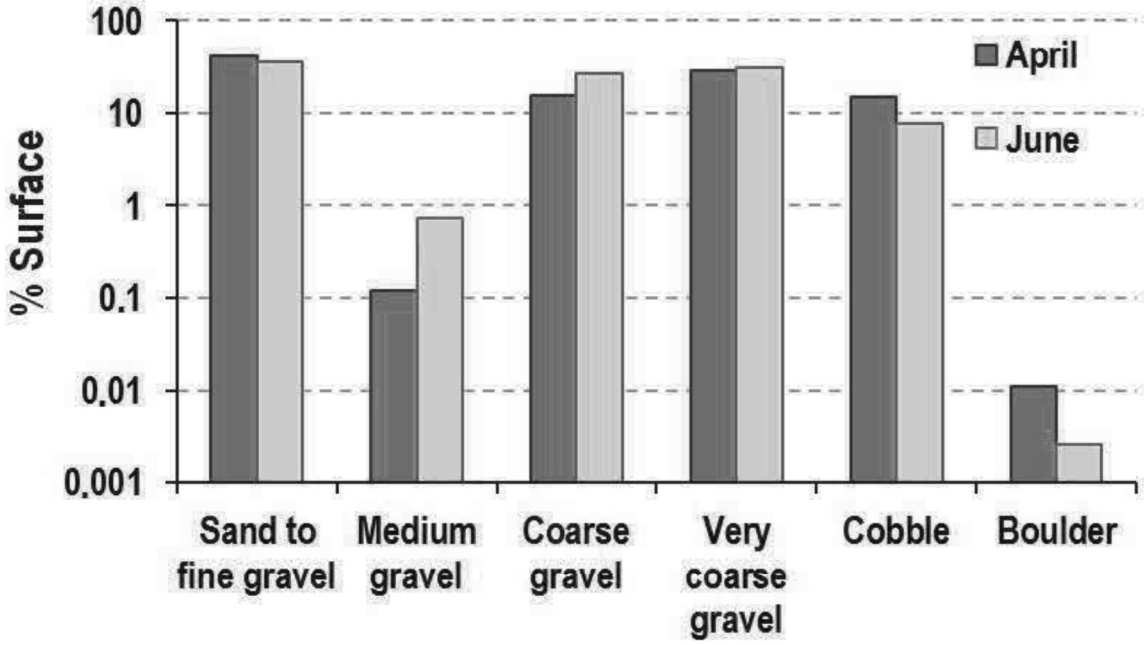
100
10
1
0.1
0.01
0.001
% Surface
April
June
Sand to fine gravel
Medium gravel
Coarse gravel
Very coarse gravel
Cobble
Boulder

Figure 12

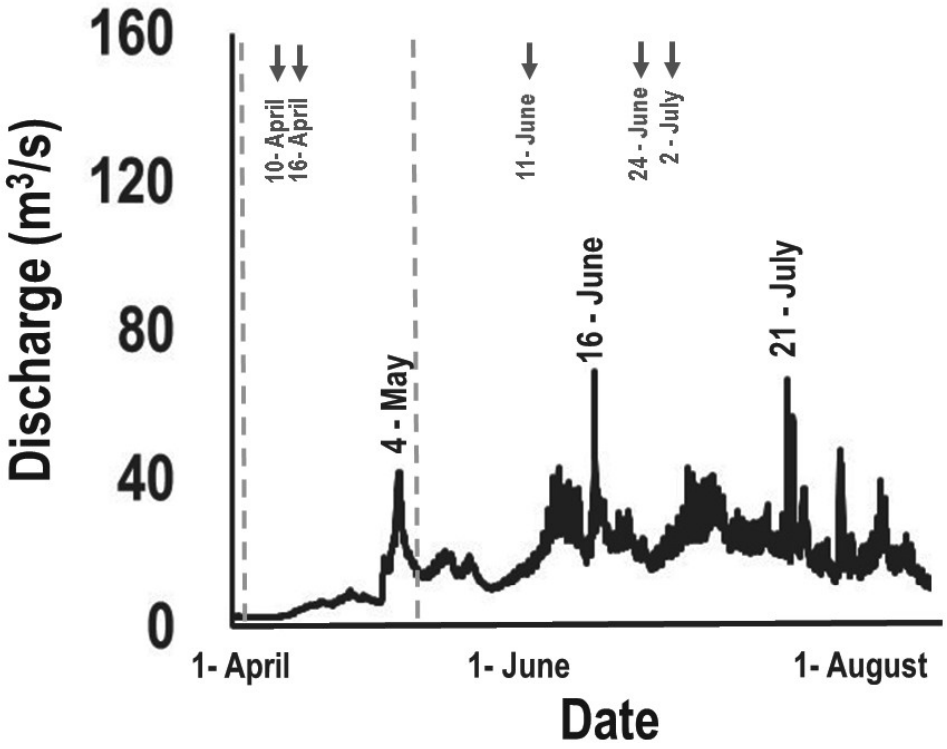
160
120
80
40
0
Discharge (m3/s)
10- April
16- April
4 - May
11- June
16 - June
24 - June
2 - July
21 - July
1- April
1- June
1- August
Date

Figure 13

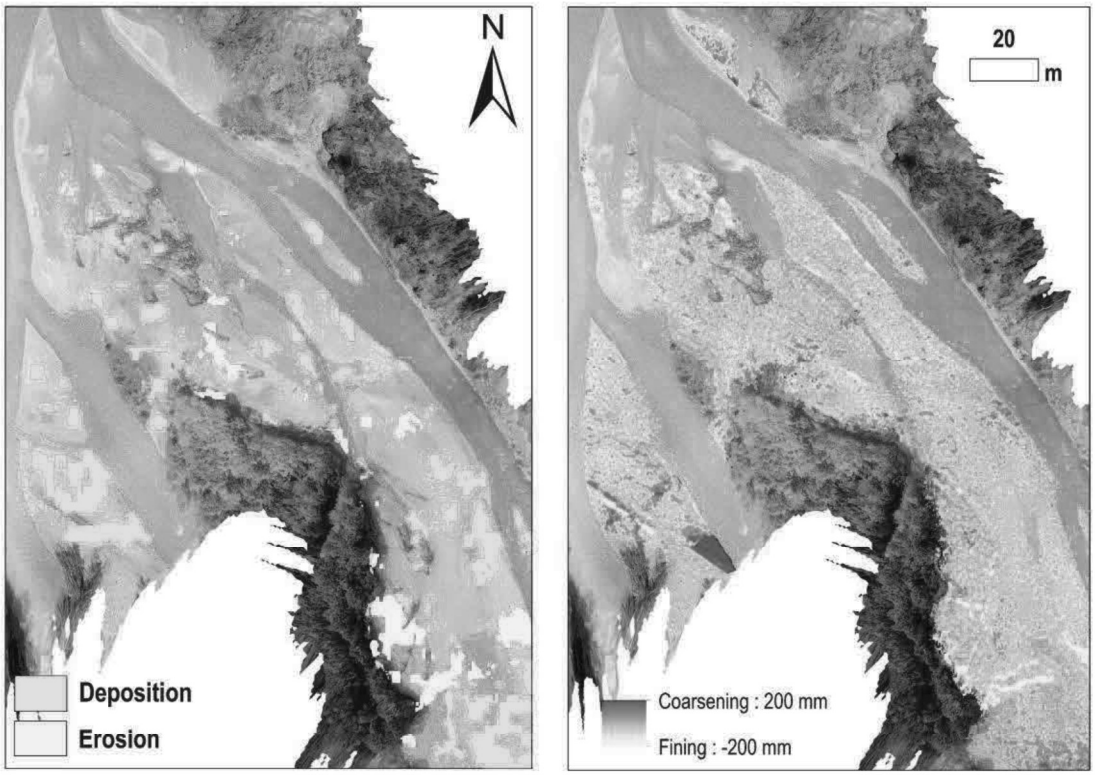

Figure 14

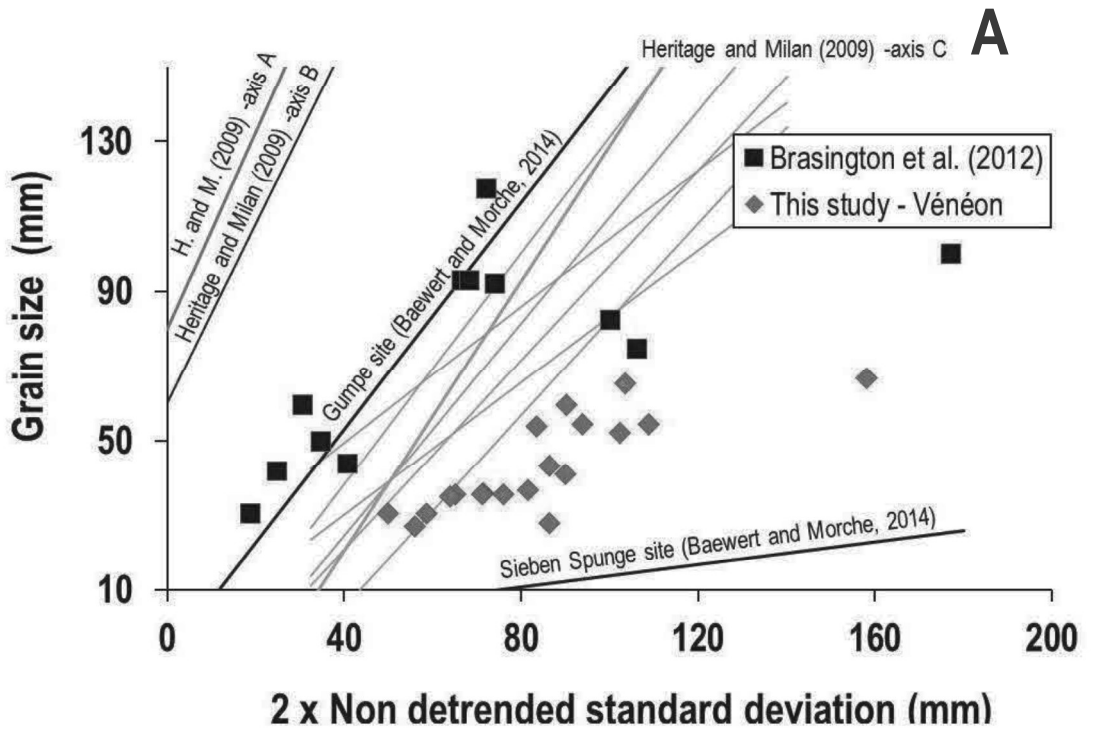
A
Heritage and Milan (2009) -axis C
H. and M. (2009) -axis A
Heritage and Milan (2009) -axis B
Gumpe site (Baewert and Morche, 2014)
Sieben Spunge site (Baewert and Morche, 2014)
Brasington et al. (2012)
This study - Vénéon
Grain size (mm)
130
90
50
10
0
40
80
120
160
200
2 x Non detrended standard deviation (mm)

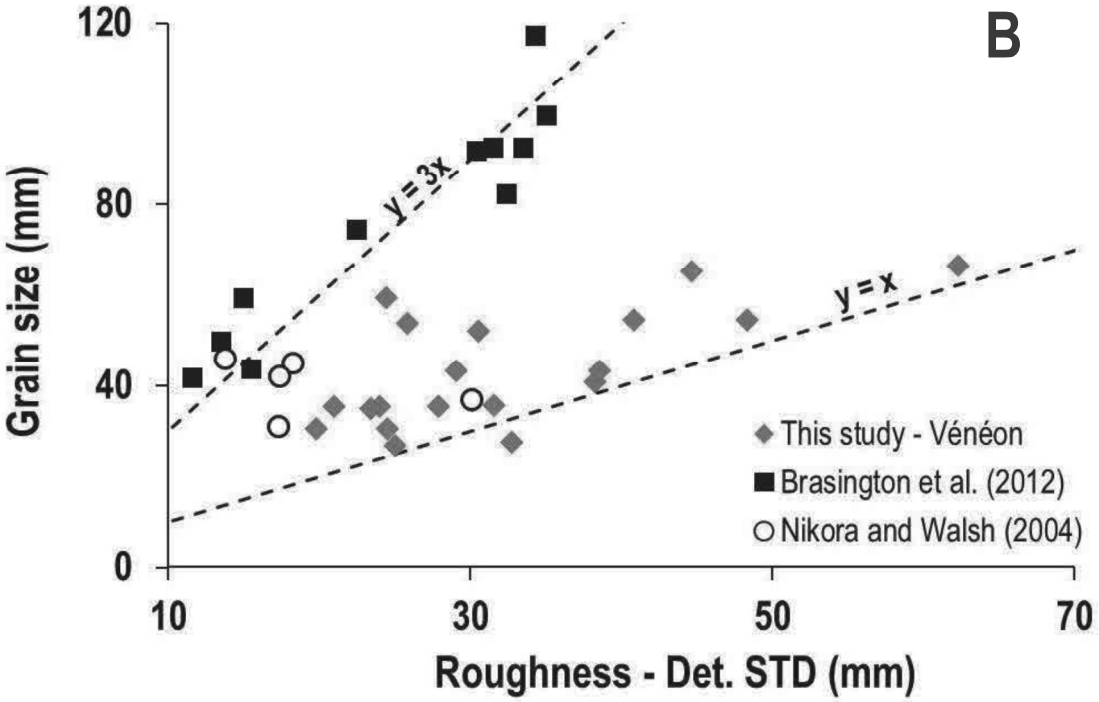
B
y = 3x
y = x
This study - Vénéon
Brasington et al. (2012)
Nikora and Walsh (2004)
Grain size (mm)
120
80
40
0
10
30
50
70
Roughness - Det. STD (mm)